# Investigations of thermonuclear bursts from 4U 1323–62 using NICER

**M.Sc. Thesis**

By

**Vikrant Someshwar Londhe**

**Discipline of Astronomy, Astrophysics and Space Engineering**

**INDIAN INSTITUTE OF TECHNOLOGY INDORE**

**June 5, 2021**

# Investigations of thermonuclear bursts from 4U 1323–62 using NICER

**M.Sc. Thesis**

*Submitted in partial fulfillment of the requirements for the awards of the degree*
***of***
**Master of Science**

by

**Vikrant Someshwar Londhe**

**Discipline of Astronomy, Astrophysics and Space Engineering**

**INDIAN INSTITUTE OF TECHNOLOGY INDORE**

**June 5, 2021**

# INDIAN INSTITUTE OF TECHNOLOGY INDORE

## CANDIDATE'S DECLARATION

I hereby certify that the work which is being presented in the thesis entitled '**Investigations of thermonuclear bursts from 4U 1323–62 using NICER**' in the partial fulfillment of the requirements for the award of the degree of **MASTER OF SCIENCE** and submitted in the **Department of Astronomy, Astrophysics and Space Engineering, Indian Institute of Technology Indore**, is an authentic record of my own work carried out during the time period from 25/July/2019 to 09/June/2021. Thesis submission under the supervision of **Dr. Manoneeta Chakraborty**, Assistant Professor.

The matter presented in this thesis has not been submitted by me for the award of any other degree of this or any other institute.

09/06/2021

**Signature of the student with date**
**(Vikrant Someshwar Londhe)**

---

This is to certify that the above statement made by the candidate is correct to the best of my knowledge.

Manoneeta Chakraborty
09/06/2021

Signature of the Supervisor of M.Sc. thesis (with date)
**MANONEETA CHAKRABORTY**

---

**Vikrant Londhe** has successfully given his M.Sc. Oral Examination held on **09/06/2021**.

Manoneeta Chakraborty

Signature(s) of Supervisor(s) of MSc thesis
Date: 09/06/2021

Suman Majumdar 10/06/2021

Convener, DPGC
Date:

Saptarshi Ghosh

Signature of PSPC Member #1
Date: 10/06/2021

Suman Majumdar 10/06/2021

Signature of PSPC Member #2
Date:

S. Das

Signature of PSPC Member #3
Date: 10/06/2021

Signature of M.Sc coordinator
Date: 10-06-2021

Signature of Head of the department
Date: 10/06/2021

---

## Abstract

Compact objects are generally observed in the binaries. When accretion takes place on the compact object from the companion star in the binary system, fuel accumulates on the surface of the star and after a considerable thick layer is formed it burns unstably giving a thermonuclear burst which lasts for 10 to 100 seconds. This thesis discusses the type-I thermonuclear bursts. The source 4U 1323–62 was used for investigating properties of the thermonuclear bursts. The observations were taken from NICER X-ray telescope which has good time resolution and the energy range where it is sensitive is ideal for study of bursts. The instrument used is the X-ray timing instrument (XTI) on-board NICER. We have scanned the light curves from entire public archival NICER data of 4U 1323–62 and searched for thermonuclear bursts. We detected 11 bursts. We have generated time-resolved spectra for every burst, used blackbody model for spectral fitting and studied how its parameter changes with time. We have also presented the energy resolved light curves for one of the bursts.

# Contents

# List of Figures

# List of Tables

# Chapter 1

# Introduction

## 1.1 Compact objects

Compact objects, the densest objects in the universe, are remnants created following the life cycle of a star.When the main-sequence stars, that fuses hydrogen into helium in their core, run out of fuel, the thermal pressure released due to fusion that was balancing the gravitational pressure ceases to exist. This leads to the collapse of the main sequence star. The collapse continues till the electron degeneracy pressure comes into play which balances the gravitational pressure and stops further collapse. This is the case when a white dwarf is created. Generally, the stars of roughly 1 to 7 $M_{\odot}$ end up becoming the white dwarfs. When the mass of the star is in range of 8 to 20 $M_{\odot}$, the electron degeneracy pressure cannot hold the gravitational pressure, and it leads to further collapse till the neutron degeneracy pressure comes into the picture which the balances the inward gravitational pressure. These types of compact objects are called neutron stars. After collapse, it becomes a star of mass 1.4 $M_{\odot}$ and 10 km radius (both values are an approximation).

## 1.2 X-ray binaries

A binary system is formed when two stars are gravitationally bound to each other and orbit around a common centre of mass. X-ray binaries are a class of binary stars that have a compact star along with the main sequence star or another compact object. They are luminous in X-rays. Around the binary system there are equipotential surfaces which connects all points where potential is the same. Also, there are points where force due to the gravity of two stars and centrifugal force are balanced. Such points are called as Lagrangian points. The equipotential surface which is called as Roche lobe is a critical equipotential surface around a star, beyond which the material is out of the gravitational influence of the star. Roche lobe overflow occurs when one star grows beyond the Roche lobe and since the Roche lobe is connected by the Lagrangian point which is unstable equilibrium the material crosses via that point and enters the gravitational influence of the companion star. The intrinsic angular momentum which the material carries with it causes a disk to be formed around the compact object rather than falling directly. That disk is called as an accretion disk.

In Low mass X-ray binaries (LMXB), the mass of the companion star is approximately 1 $M_{\odot}$. Since the companion stars in the LMXB have less mass, they live longer so LMXBs can be very old systems. An LMXB is born when either a direct binary system comes into existence or when a star gets bound to a compact object during the close encounter (this happens in a place where stellar density is higher). Figure 1.1 shows various components of X-ray binary system such as corona, accretion disk, Roche lobe, accretion stream as well as their respective radiation in different wavelength bands.

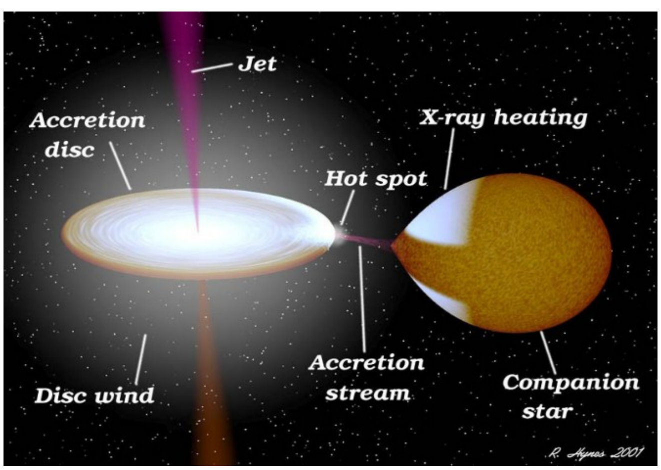


Figure 1.1: X-ray Binary and its components. (Credit: NASA/R. Hynes)

## 1.3 Motivation

The compact objects are one of the densest objects existing in the universe. Their densities are more than nuclear densities ranging up to $2.3 \times 10^{17}$ kg/m$^2$ 19 (https://astronomy.swin.edu.au/cosmos/N/Neutron+Star). This gives us the chance to study the behaviour of matter in the densities higher than the nuclear densities. The compactness of these objects makes them the best place to study the general theory of relativity in the strong gravity regime (van der Klis et al. 2004). The high magnetic fields of $10^8$-$10^{15}$ Gauss (Reisenegger et al. 2001) makes them perfect to study the behaviour of matter in the high magnetic field.

## 1.4 Spectral states

As the accretion rate onto the compact object changes, the LMXBs show wide variation in the intensity of the radiation. During these active phases, as the accretion rate changes, significant change in radiative behaviour and intensity is observed. We can study the evolution of X-ray binary with changes in accretion rate by studying these changes in radiative behaviour as well as intensity.

The primary step to study this LMXB evolution is through the CD (colour-colour diagram) and HID (Hardness intensity diagram) diagram. The ratio of intensities in the two energy bands of X-ray is called as colour. Colour Colour diagram are the diagrams where hard X-ray colour is plotted versus soft X-ray colour. Figure 1.2 shows the path traced by the neutron star LMXB in the CD diagram. In HID diagram we plot hardness versus intensity or hard colour vs intensity plot. As the LMXB evolves it traces the path in CD/HID diagram and the path of the source in these diagrams represent the spectral evolution of the source (M. van der Klis et al. 2004). Sources generally have two distinct spectral states i.e., low/hard and high/soft states in which the source exists and in between these two states there are also intermediate states. Low/Hard state (Figure 1.3 lower panel) is non-thermal (power law dominated), source of it is corona and is due to the inverse Compton effect arising from the interaction of photons from accretion

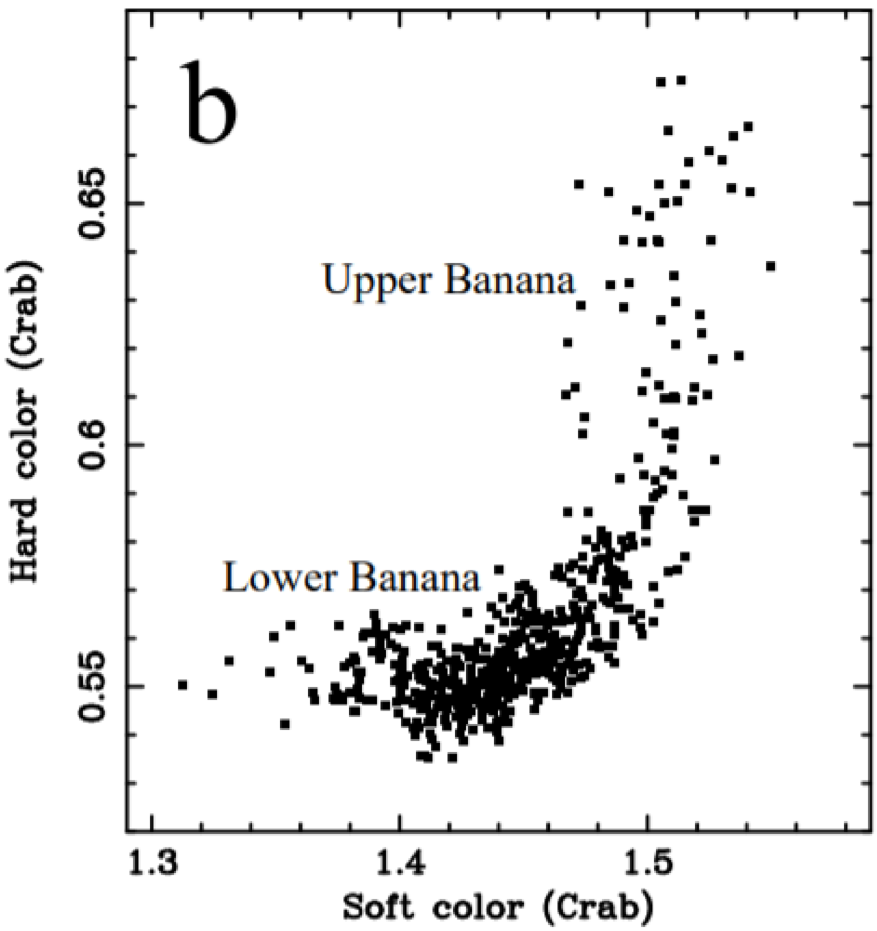


Figure 1.2: CD diagram of the neutron star LMXB GX 9+1 (M. van der Klis et al. 2004).

disk with the corona. Minor components include thermal component and reflection component (the relativistic Fe lines which occur due to reflection in the inner disk). Disk temperature is $1.1 - 3.6 \times 10^6$K and total emission is primarily in the hard X-rays. Whereas, in High/soft (Figure 1.3 upper panel) state thermal radiation dominates which is generated from the accretion disk. Minor component is the non-thermal emission. The X-ray emission which dominates here is soft X-ray emission of 1 keV approximately. The disk temperature in this case is approximately $10^7$ K (Remillard & McClintock et al. 2006).

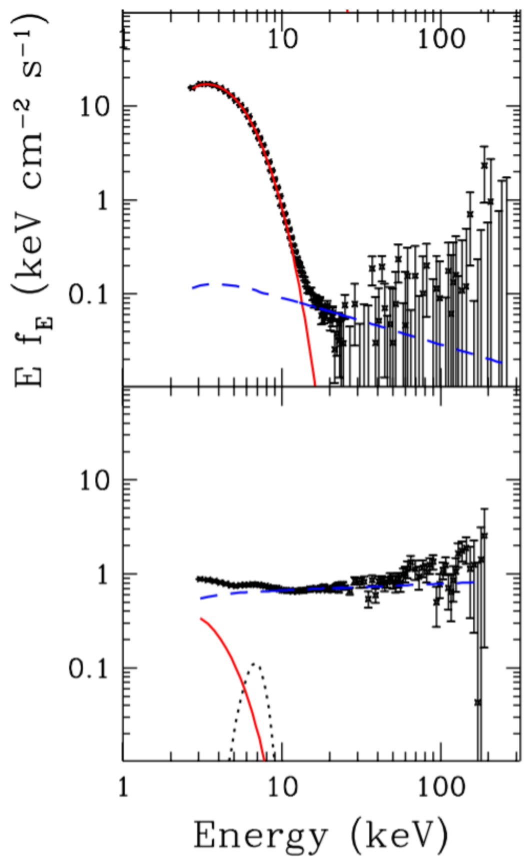


Figure 1.3: The upper panel shows the spectrum in the high/soft (thermal) state and lower panel shows the spectrum in the low/hard (non-thermal) state. Thermal component — Red solid line, power law — Blue dashed line, relativistically broadened Fe line — Black dotted line (McClintock & Remillard 2006).

# Chapter 2

# Thermonuclear burst

In low mass X-ray binaries with neutron stars as a compact object, the type-I thermonuclear burst occurs as the accreting material mostly containing H and He forms a layer on the surface of the neutron star and when it becomes approximately a meter thick, the unstable thermonuclear burning occurs which is started due to the compression and temperature generated due to it in the inner part of layers. After its ignition, it spreads in all parts of the neutron star and is manifested as a sudden burst of energy. The energy released from accretion of a hydrogen atom on to the neutron star surface is far greater than the energy released via thermonuclear reaction (fusion), so these bursts would have not been visible if the rate of nuclear reaction was similar to the rate of accretion. Sudden release of all energy in short time, due to unstable runaway thermonuclear reaction, is what makes it visible (Strohmayer et al. 2003). Thermonuclear burst has a rise time of rise time of 1-10 s and lasts up to 10-100 s approximately. They show a fast rise and exponential decay profile. Generally, the slow rise and decay of the intensity is due to mixed burning of hydrogen/helium fuel and faster rise and fall times are associated with helium burning. We can imagine this phenomenon as sudden heating due to the X-ray burst following it the exponential cooling of ashes. Since the thermonuclear bursts are brighter than non-burst emission making it easier to study due to less background noise. Since the bursts originate directly from the surface so the effects intrinsic to the neutron star can be distinguished. The timing and spectral features of the bursts can be used to constraint mass, radius, and spin frequency of the neutron. Through investigation of thermonuclear bursts, we would be able to study the physics under extreme conditions such as extreme gravity, high magnetic field as well as energy generation via nuclear reactions under such extreme cases. It can be used to constrain composition of accreted matter and consequent nuclear burning on neutron star can also be studied.

The intensity of the burst, its frequency with which it reoccurs and the time for which it lasts depend on the composition of the accreted matter. The fuel left from the previous ignition also decides the above-given parameters (Galloway et al. 2006). After the accreted hydrogen and helium has become part of the neutron star, hydrostatic compression of the accumulated matter layer takes place and thermonuclear reaction is initiated when the required density and temperature is reached. The compression rate depends on the accretion rate per unit area.

At the temperatures exceeding $10^7$ K hydrogen burns via CNO cycle. In this $\beta$ decay is prominent. When the temperature reaches approximately $8 \times 10^7$ K the proton capture becomes prominent than $\beta$ decay hence the Hot CNO cycle follows. This happens when accretion rate per unit area is greater than 900 g cm$^{-2}$ sec$^{-1}$.

For accretion rates per unit area lower than this, the hydrogen burns unstably, which can cause a burst to occur. The slow burning of hydrogen during accumulation causes He/H to burn simultaneously at mass accretion rate per unit area greater than $2 \times 10^3$ g cm$^{-2}$ sec$^{-1}$ and at these rates the fluid is compressed till the helium ignition condition is reached and still all hydrogen is not burned. The Helium burning is too sensitive to temperature at temperature less than $5 \times 10^8$ K which causes burst to occur. At even higher accretion rate per unit area helium burning becomes stable (Strohmayer et al. 2003).

For a pure helium flash, the fuel burning rate is rapid and many a time causes photospheric radius expansion. Figure 2.1 is a case which shows the photospheric radius expansion. When H and He both are present, temperature due to the thermal instability can trigger the rp process (rapid proton capture process). In rp process, consecutive proton capture takes place by the seed nuclei to produce higher and higher elements. This starts when helium flash heats the gas and a breakout reaction occurs. This reaction removes catalysts out of the CNO cycle loop and causes rp burning for hydrogen. Mixed H/He flash lasts longer than just helium flash (Strohmayer et al. 2003).

The few key points regarding the thermonuclear burst are rise times are shorter than decay time. The burst profiles are shorter at high energies. The burst radiation can be represented by a blackbody emission of temperature 2-3 keV. Using bolometric flux and temperature, the neutron star radius can be found. For a few cases, the blackbody temperature of the burst spectrum was slightly higher than what it should have been at their Eddington luminosity, this might be spectral hardness due to the Compton scattering in the atmosphere is one of the possibility we can consider (Strohmayer et al. 2003). By observing the spectral evolution of the blackbody spectrum during

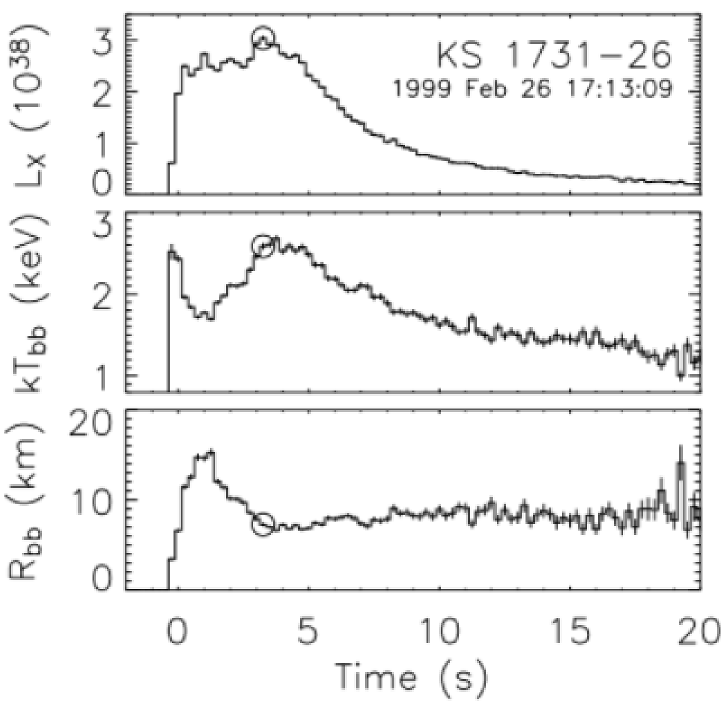


Figure 2.1: Spectral evolution during a thermonuclear burst (Galloway et al. 2008).

the thermonuclear burst (Figure 2.1), we can study ignition and subsequent emission mechanisms. Also, the blackbody radius can help us estimate the radius of a neutron star.

The thermonuclear burst exists in all the spectral states and their nature changes based upon the source spectral state (Figure 2.2 and Figure 2.3). This behaviour can be used to study the ignition mechanism and accretion-ignition connection.

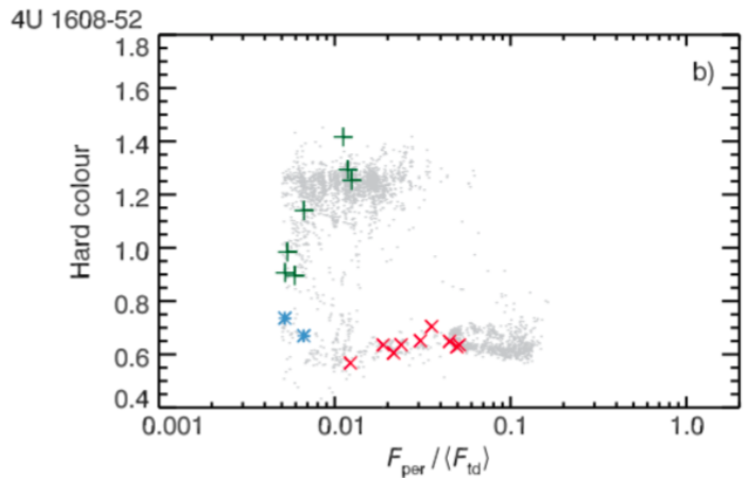


Figure 2.2: Plot showing the presence of thermonuclear bursts in the different spectral states of the source. The X-axis shows the normalized persistent flux and the Y-axis shows the hard colour. The green symbols indicate bursts in the hard/low (non-thermal) state, the blue symbol indicate bursts in the intermediate source spectral state and the red symbols indicate the bursts in the high/soft (thermal) state (Kajava et al. 2014).

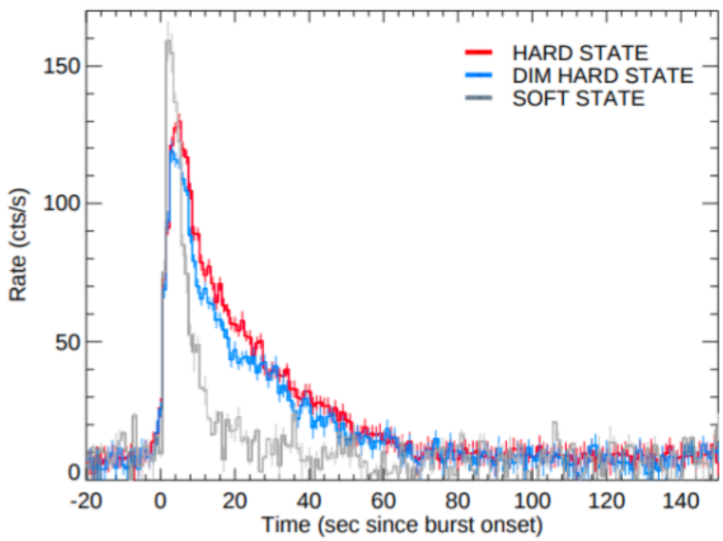


Figure 2.3: Thermonuclear burst profile in the different source spectral states show different profile features. Red - burst in hard state, blue - burst in dim hard state, grey - burst in soft state (Sánchez-Fernández et al. 2020).

## 2.1 Source

The source 4U 1323-62 was first detected by UHURU satellite. It is located 0.3° above the galactic plane and in the direction of approximately 53° from galactic centre. EXOSAT was used to observe faint UHURU sources in which a thermonuclear burst was detected. Detection of thermonuclear burst in the source made us to place it in the category of neutron star LMXB (M. van der Klis et al. 1985). Also, a periodic dip was detected, that is caused when a companion star ellipses the source, which helped to estimate its period (Bhulla et al. 2020). From the nature of the bursts, its approximate distance from earth was found to be 10-20 kpc (Parmar et al. 1989). This source was extensively observed by NICER and the NICER data will help us explore more about the source.

# Chapter 3

# Instrument

The Neutron star Interior Composition Explorer (NICER) telescope is the X-ray telescope which is on the International Space Station (90 minutes orbit time) is used in measuring the X-ray pulse profiles from neutron star X-ray pulsars, accreting compact binaries, flaring sources, stars, supernova remnants, galaxy clusters, etc. (https://heasarc.gsfc.nasa.gov/docs/nicer/mission_guide/).

It has a bandpass of 0.2 to 12 keV and absolute precision of timing less than 300 ns. The effective area at 1.5 keV is 1900 $cm^2$. The spectral resolution is moderate and varies in the range between 6-80 from 0.5 keV to 8 keV.

The instrument used here is X-ray timing instrument (XTI) on-board NICER which is shown in Figure 3.2. The XTI detector used on NICER is SDD (silicon drift detector). There are 56 X-ray concentrator optics and SDD pairs. They collect the X-rays from a large geometric area from roughly 30 arc $mins^2$ region and focus on the SDD. Each X-ray concentrator consists of 24 nested parabolic gold-plated thin foil mirrors. X-ray reflected from these are concentrated on the 2 mm aperture of the focal plane module. Focal plane module (FPM) contains SDD. The active area of FPM is restricted to a 2 mm aperture to minimize diffuse-sky background and source confusion. All the above properties not only make this telescope ideal for the study of pulsars but also ideal for the study of a wide variety of X-ray sources (e.g., accreting compact binaries in our case). 8 FPM are controlled by each measurement and power unit (MPU). There are 7 MPUs labelled from 0-6 and each MPU has 8 FPM. The data from individual FPM can be analysed but generally, all the MPU are merged.

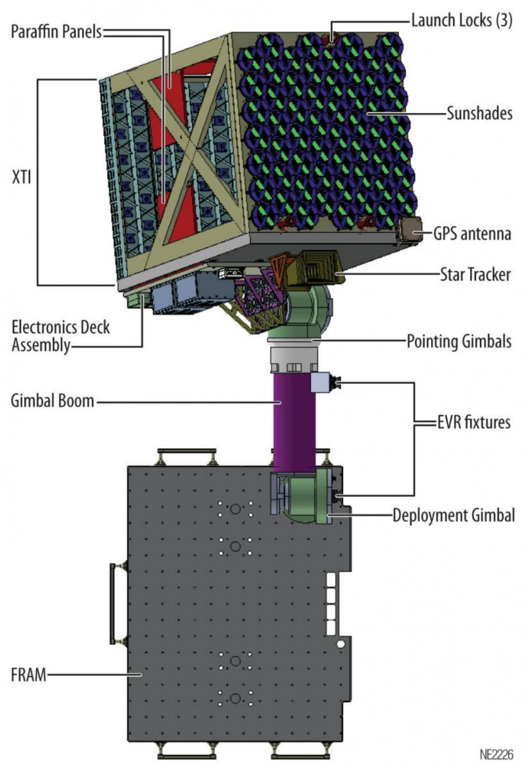


Figure 3.1: NICER telescope (https://heasarc.gsfc.nasa.gov/docs/nicer/)

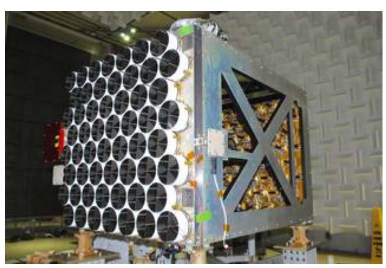

Figure 3.2: X-ray timing instrument (https://www.nasa.gov/content/about-nicer)

# Chapter 4

# Observation and data processing

## 4.1 Observation

The data used in this work are all archival public NICER data of the source 4U 1323-62 corresponding to 120 observations. Out of the total observations, we were able to generated light curve for 92 observations which are mentioned in the Table 4.1. Remaining data was not reliable for plot generation since it showed zero GTI.

| Observation ID | Date & Time (UTC) (YYYY-MM-DDThh:mm:ss) | Exposure (seconds) |
|---|---|---|
| 1105010101 | 2017-08-16T17:08:40 | 12 |
| 1105010102 | 2017-08-17T07:03:40 | 0 |
| 1105010104 | 2017-09-30T00:21:00 | 14068 |
| 1105010105 | 2017-10-01T00:05:41 | 10633 |
| 1105010106 | 2017-10-02T00:14:00 | 827 |
| 1105010107 | 2017-10-03T02:23:48 | 4699 |
| 1105010108 | 2017-10-04T00:06:40 | 15517 |
| 1105010109 | 2017-10-05T00:39:20 | 5381 |

Table 4.1: Complete list of public archival NICER observations of 4U 1323–62 which are studied in this work.

| | | |
|---|---|---|
| 1105010125 | 2017-11-26T01:00:09 | 637 |
| 1105010133 | 2017-12-17T11:14:09 | 470 |
| 1105010134 | 2017-12-19T06:49:00 | 8235 |
| 1105010135 | 2017-12-22T06:53:16 | 4239 |
| 1105010136 | 2017-12-23T15:33:00 | 5047 |
| 1105010137 | 2017-12-26T00:33:43 | 1099 |
| 1105010138 | 2018-01-08T00:00:40 | 10831 |
| 1105010139 | 2018-01-09T09:49:07 | 7678 |
| 1105010140 | 2018-01-10T04:19:11 | 18880 |
| 1105010141 | 2018-01-11T00:18:20 | 6675 |
| 1105010142 | 2018-01-12T04:04:57 | 14812 |
| 1105010143 | 2018-01-14T20:59:29 | 7194 |
| 1105010144 | 2018-01-15T03:19:11 | 4911 |
| 1105010145 | 2018-01-16T02:27:13 | 12520 |
| 1105010146 | 2018-03-09T18:47:40 | 3616 |
| 1105010147 | 2018-12-20T12:02:00 | 5113 |
| 1105010148 | 2018-12-1T23:31:00 | 4397 |
| 1105010149 | 2018-12-22T10:21:00 | 10746 |
| 1105010151 | 2019-01-05T02:46:20 | 407 |
| 1105010152 | 2019-01-07T22:42:40 | 1281 |
| 1105010153 | 2019-01-08T00:15:20 | 0 |
| 1105010154 | 2019-01-10T15:09:57 | 18371 |
| 1105010155 | 2019-01-14T05:34:00 | 13347 |
| 1105010156 | 2019-01-16T17:51:40 | 2681 |
| 1105010157 | 2019-01-17T01:34:56 | 10088 |

Table 4.1: Complete list of public archival NICER observations of 4U 1323–62 which are studied in this work.

| | | |
|---|---|---|
| 1105010158 | 2019-01-18T04:03:00 | 13418 |
| 1105010159 | 2019-01-23T09:07:57 | 0 |
| 1105010160 | 2019-02-14T01:51:40 | 6797 |
| 1105010161 | 2019-02-15T11:55:20 | 4279 |
| 1105010162 | 2019-02-16T18:52:20 | 945 |
| 1105010163 | 2019-02-17T07:16:20 | 1920 |
| 1105010164 | 2019-02-27T16:58:45 | 9803 |
| 1105010165 | 2019-02-28T06:55:55 | 9406 |
| 1105010166 | 2019-03-01T10:45:51 | 4605 |
| 2105010101 | 2019-04-30T10:14:00 | 1493 |
| 2105010102 | 2019-05-01T07:53:43 | 9767 |
| 2105010103 | 2019-05-06T11:36:00 | 503 |
| 2105010104 | 2019-05-11T12:20:06 | 12382 |
| 2105010105 | 2019-05-12T00:42:45 | 8556 |
| 2105010106 | 2019-05-16T23:13:40 | 2293 |
| 2105010107 | 2019-05-18T03:07:20 | 1792 |
| 2105010108 | 2019-05-19T06:50:20 | 6659 |
| 2105010109 | 2019-05-22T21:43:24 | 422 |
| 2105010110 | 2019-05-23T19:24:51 | 0 |
| 2105010111 | 2019-07-14T22:05:00 | 4162 |
| 2105010112 | 2019-07-15T01:11:20 | 62415 |
| 2105010113 | 2019-07-16T01:47:20 | 18234 |
| 2105010114 | 2019-07-17T01:20:16 | 23848 |
| 2105010115 | 2019-07-18T03:38:20 | 16208 |
| 2105010116 | 2019-07-19T07:33:40 | 2975 |

Table 4.1: Complete list of public archival NICER observations of 4U 1323–62 which are studied in this work.

| | | |
|---|---|---|
| 2105010117 | 2019-07-20T21:50:40 | 18863 |
| 2105010118 | 2019-07-22T20:15:57 | 5964 |
| 2105010119 | 2019-07-23T00:50:40 | 5434 |
| 2105010120 | 2019-07-24T06:16:41 | 23737 |
| 2105010121 | 2019-07-25T02:24:52 | 3818 |
| 2105010122 | 2019-07-26T14:01:08 | 102 |
| 2105010123 | 2019-07-27T03:56:48 | 1961 |
| 2105010124 | 2019-07-28T13:56:20 | 0 |
| 2105010125 | 2019-08-26T08:56:40 | 14832 |
| 2105010126 | 2019-08-30T18:01:40 | 3208 |
| 2105010127 | 2019-09-01T10:11:00 | 15048 |
| 2105010128 | 2019-09-02T03:12:40 | 4742 |
| 2105010129 | 2019-09-03T02:27:39 | 18194 |
| 2105010130 | 2019-09-05T00:51:34 | 17743 |
| 2105010131 | 2019-09-09T20:56:40 | 12377 |
| 2105010132 | 2019-09-23T11:32:20 | 2104 |
| 2105010133 | 2019-09-25T02:20:40 | 1024 |
| 2105010134 | 2019-09-29T17:39:40 | 691 |
| 2105010139 | 2020-01-06T02:33:40 | 12126 |
| 2105010140 | 2020-01-08T16:26:38 | 32773 |
| 2105010141 | 2020-01-09T00:10:38 | 155615 |
| 2105010142 | 2020-01-10T00:57:40 | 88481 |
| 2105010144 | 2020-01-12T00:52:20 | 39091 |
| 2105010145 | 2020-01-13T04:47:57 | 32097 |
| 2105010146 | 2020-01-14T00:55:17 | 25614 |

Table 4.1: Complete list of public archival NICER observations of 4U 1323–62 which are studied in this work.

| | | |
|---|---|---|
| 2105010147 | 2020-01-15T00:07:57 | 41847 |
| 2105010148 | 2020-01-16T00:54:37 | 32159 |
| 2105010149 | 2020-01-17T01:41:36 | 30523 |
| 2105010150 | 2020-01-18T00:57:00 | 27727 |
| 2105010151 | 2020-01-19T00:11:20 | 41821 |
| 2105010152 | 2020-01-20T00:59:00 | 31558 |
| 2105010153 | 2020-01-21T00:24:40 | 17457 |
| 2105010154 | 2020-01-22T01:03:32 | 19342 |
| 2105010155 | 2020-02-08T01:43:40 | 840 |
| 2105010156 | 2020-02-12T11:29:00 | 2611 |
| 2105010157 | 2020-02-13T12:11:20 | 11751 |
| 2105010158 | 2020-02-14T00:37:00 | 23977 |
| 2105010159 | 2020-02-14T23:57:00 | 12272 |
| 2105010160 | 2020-02-17T01:14:20 | 9904 |

## 4.2 Data reduction

In this project Heasoft (version- 6.28) software is used for the data analysis. The raw data is processed at Science Mission Operation Center and delivered to the High Energy Astrophysics Science Archive Research Center (HEASARC). Science data is organized by observation in which observation is defined as data for a single target collected by NICER detector, XTI over a period of day.

The observation directory, identified by a specific observation ID, contains raw data from all the MPUs along with the housekeeping data. Apart from these, it also includes auxiliary data like attitude file, orbit file etc. are also present which are required for advanced science analysis.

The NICER data can be divided into the following classes depending on

the level of processing applied:
Level 1: data delivered to archive, uncalibrated and divided into MPU
Level 2: calibrated and unscreened and all MPU merged
Level 2a: Level 2 data with screening performed
Level 3: Final products, these are the standard products like light curve, spectra etc. used for science analysis.

NICERDAS is a set of the NICER specific tools which comes with Heasoft is used for data reduction. On the unfiltered fits files in level one, we performed corrections to generate the level two files using the pipeline `nicerl2`. It selects the good time intervals (GTIs) filtering for satellite and machine generated effects and provides data for further analysis, applies calibration, and merges the data from the individual MPU units.

On obtaining the Level-2 files, we used `XSelect` software to extract the event file, light curve, and spectrum.

# Chapter 5

# Results

## 5.1 Light curves

### 5.1.1 Detection of thermonuclear burst

Firstly, using NICERDAS we generated the level 2 files for 92 observations from 1105010101-1105010166 and 2105010101-2105010160.

These files were loaded in `Xselect` for generation of light curves. We have set the bin size as 1 s for each light curve. The general depiction of the light curve generated is shown in the Figure 5.1. The criterion used for identifying bursts was:- (a) An almost order of magnitude rise of intensity above the average (persistent / non-burst) level. An example of this is shown in the Figure 5.2. When the criterion (a) is met, the part of the light curve is zoomed to check if it has a fast rise and exponential decay profile which are characteristics of a typical thermonuclear burst.

The persistent photon count is non burst radiation. The example of persistent light curve is shown in Figure 5.3. The pre-burst interval is taken from 50 seconds to 100 seconds long, which must be at least 40 seconds prior to the burst. The spectrum file of the persistent is used for subtracting it from burst spectrum as a background while performing time resolved spectroscopy. The photon counts are averaged over that time interval and that average is called as persistent level, the line in green on the burst light curves (Figure 5.7). The green line is taken as the background photon count.

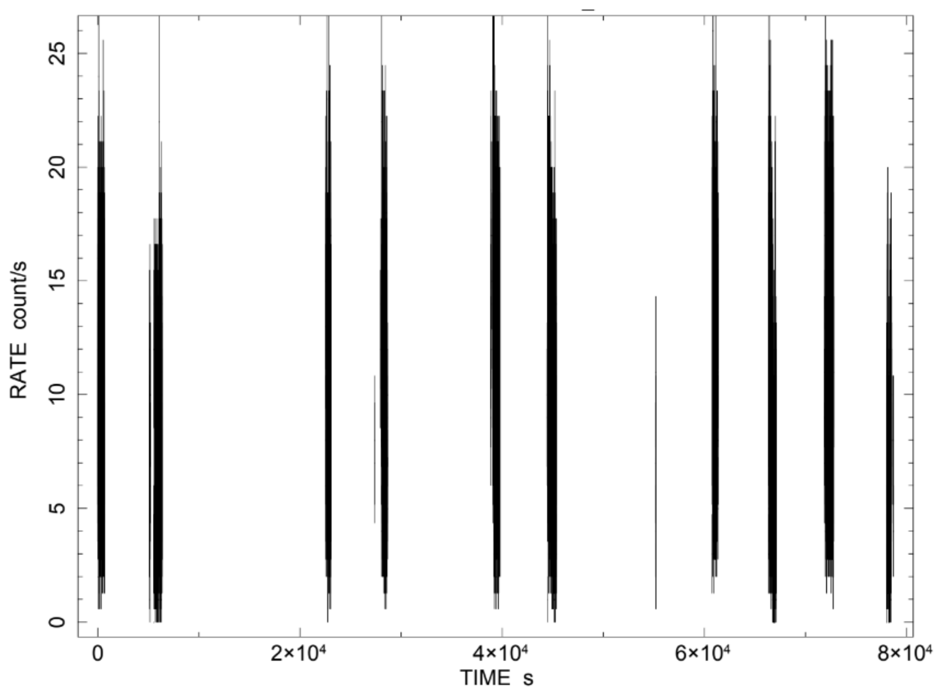


Figure 5.1: The light curve of 4U 1323–62 from observation ID 2105010112 using 1 s time bin size where no bursts were detected. This is an example of light curve of an observation having a long exposure time and no burst detection.

The cases as in Figure 5.17, where the burst starts at the very start of the orbit, in such case we averaged the persistent from previous orbit. The nature of the spectrum of persistent emission is shown in Figure 5.4.

### 5.1.2 Burst light curves

After detection of the thermonuclear burst by eye observation, we zoom the light curve to confirm its presence using second criterion (mentioned in section 5.1.1). We were able to detect 11 thermonuclear bursts from the observations listed as in the table 5.1. Figure 5.5 discusses the case where the sudden rise in the photon count is not the thermonuclear burst but the noise. The third orbit has a sharp rise in photon count. After zooming the light curve its clear that it is not the thermonuclear burst as we can see in the Figure 5.6.

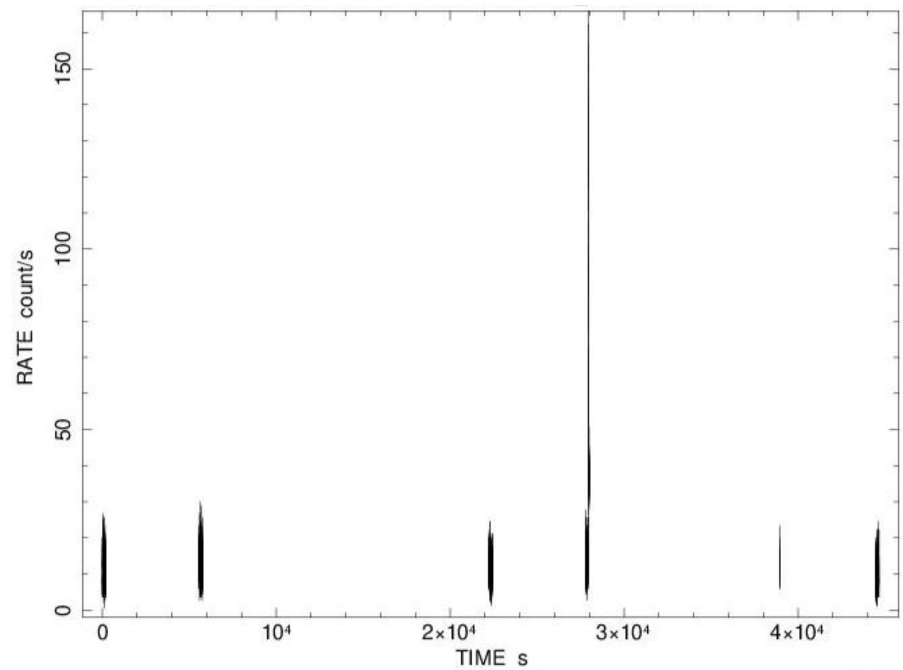


Figure 5.2: The light curve of 4U 1323–62 obtained from the observation ID 1105010142 (Observation date: 2018-01-12, Observation start time: 04:04:57 taking a time bin size of 1 s). A thermonuclear burst can be observable at ∼ 28000 s from the observation start time. The zoomed light curve of this burst is given in Figure 5.7.

We read in python the event file (.evt file located inside the subfolder named xti in observation folder) which is in FITS (FITS is a format of storing images and data in form of multidimensional array) format to generate the zoomed light curve of thermonuclear bursts. The start time is decided when there is sharp rise in intensity compared to persistent level (green line in Figure 5.7 indicates persistent level). The general criterion used to decide stop time of the burst is the point where intensity of the burst reduces to 90 % of the persistent level subtracted burst peak intensity. For the bursts which are not completely covered in the orbit, we took end of orbit as the end point of the burst.

Observing the zoomed light curves, it is clear that bursts detected in observations 1105010142 (Figure 5.7), 2105010118 (Figure 5.10), and 2105010127 (Figure 5.13) are the examples when the burst was at the end of the orbit and was not covered completely. While 2105010158 (Figure 5.17)

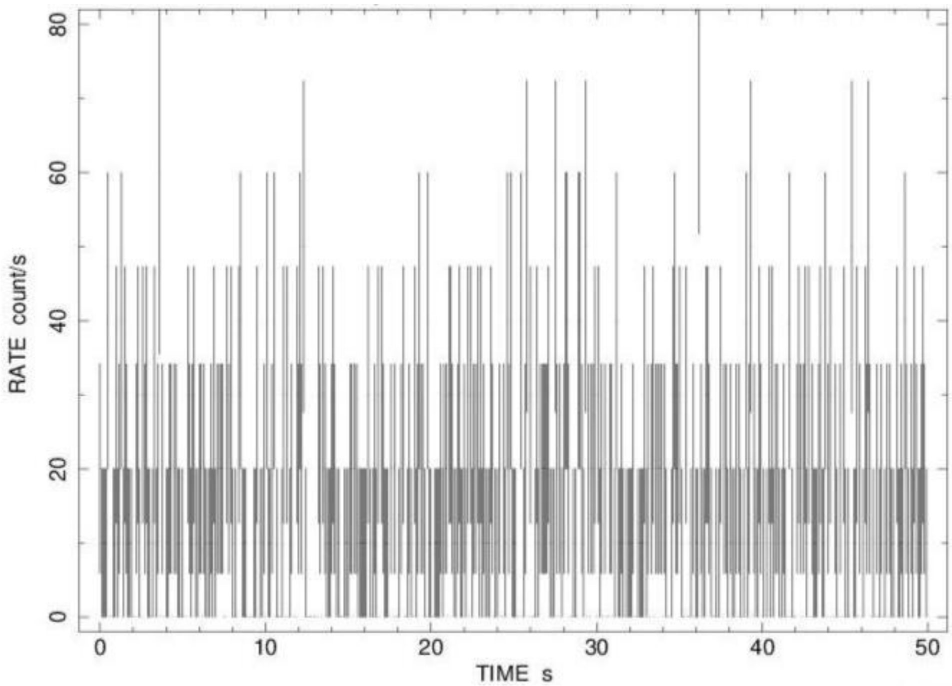


Figure 5.3: The light curve of persistent radiation obtained from a 50 s interval taken at least 40 seconds prior to burst of 4U 1323-62 from the observation ID 1105010142 (Observation date: 2019-07212, Observation start time: 20:15:57).

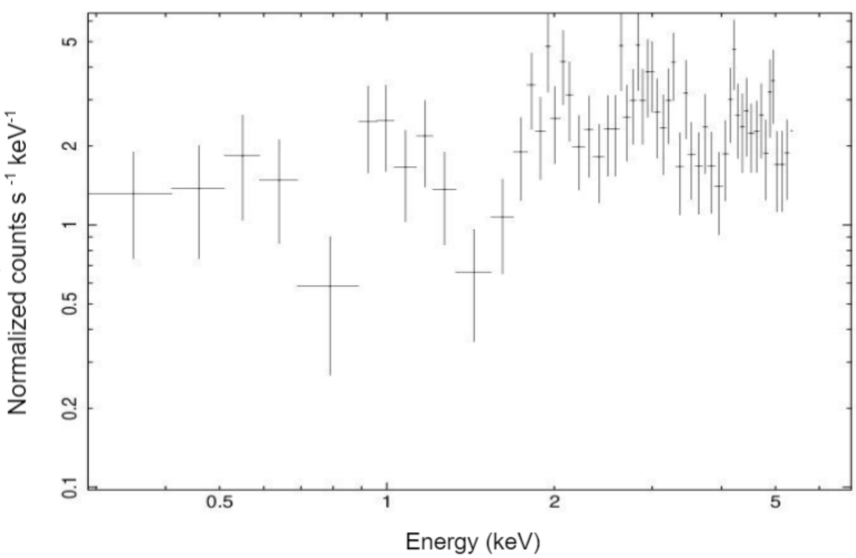


Figure 5.4: The spectrum of persistent radiation obtained from a 100 s interval taken at least 40 seconds prior to burst of 4U 1323-62 from the observation ID 1105010165. Energy range- 0.2-7.0 keV. (Observation date: 2019-02-28, Observation start time: 06:55:55).

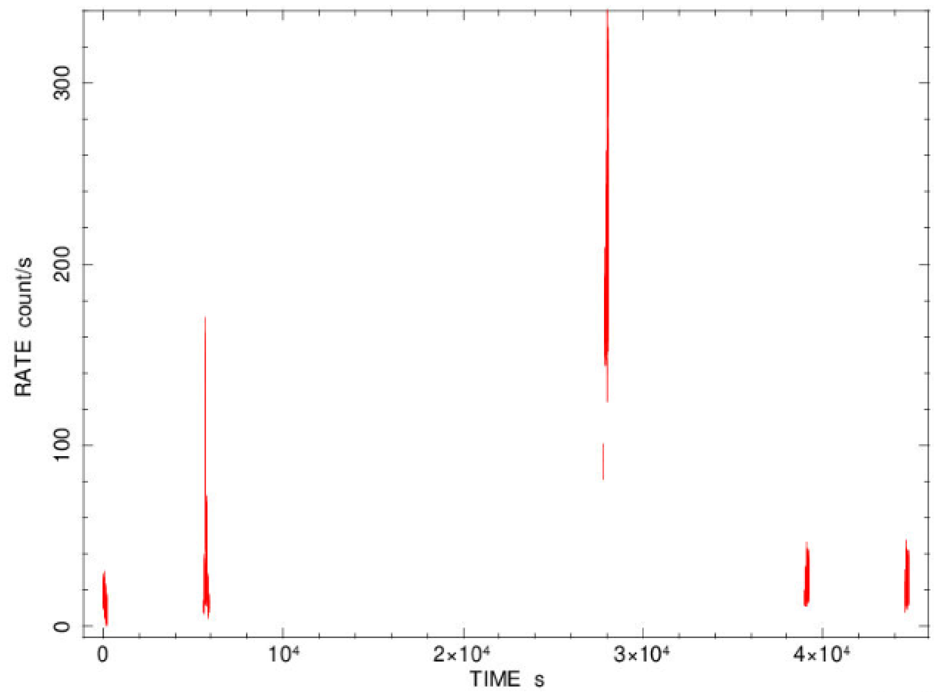


Figure 5.5: The light curve of 4U 1323–62 obtained from the observation ID 1105010165 (Observation date: 2019-02-28, Observation start time: 06:55:55 taking a time bin size of 1 s.). A thermonuclear burst can be observable at ~ 6000 s from the observation start time. There is a similar rise in intensity near ~ 28000 s. The zoomed light curve of this burst is given in Figure 5.18. The zoomed light curve of third orbit shows that noise can also generate sudden rise in photons, but is not burst as seen in zoomed light curve in Figure 5.6.

and 2105010144 (Figure 5.14) are the examples where the burst is detected at the start of orbit. Two bursts are detected from observation 1105010120 (Figure 5.11, Figure 5.12). In the first burst of observation ID 2105010120 (Figure 5.11) we can see the data gaps. Those data gaps occur when the photon count is very high and to avoid instrument damage, the instrument is shut off for a short duration.

### 5.1.3 Energy resolved burst light curve

We generated the energy resolved burst light curves in 0.2-2 keV, 2-3 keV, 3-4 keV, 4-5 keV, 5-6 keV, 6-7 keV energy ranges using `Xselect` with bin size of 1 s. Here we observe that in Figure 5.18 which is a light curve for

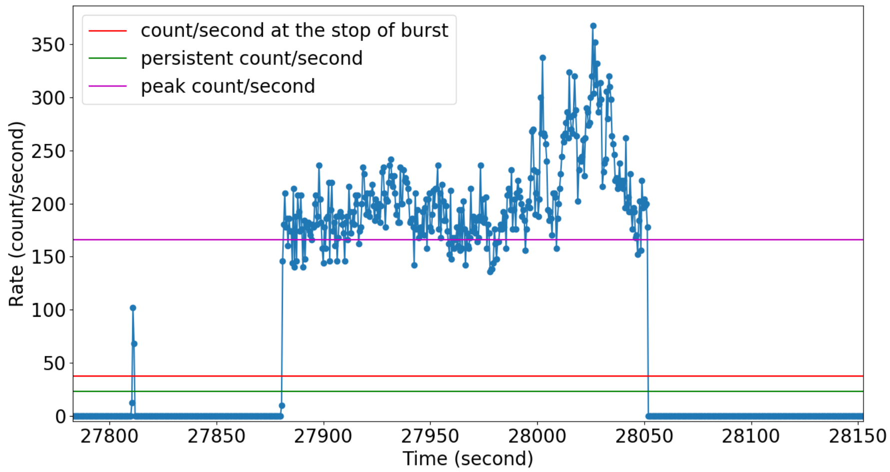


Figure 5.6: The light curve of 4U 1323–62 obtained from the observation ID 1105010165 (Observation date: 2019-02-28, Observation start time: 06:55:55 taking a time bin size of 0.5 s.). It does not show any resemblance with characteristic burst profile even when it has sharp rise in photon counts.

| Burst No. | Observation ID | Date & time (UTC) (YYYY-MM-DDThh:mm:ss) | Duration (s) | peak intensity (count/s) | persistent intensity (count/s) |
|---|---|---|---|---|---|
| 1 | 1105010142 | 2018-01-12T04:04:57 | 100 | 178 | 14.09 |
| 2 | 1105010165 | 2019-02-28T06:55:55 | 58.39 | 166 | 23.02 |
| 3 | 2105010114 | 2019-07-17T01:20:16 | 78.63 | 198 | 4.70 |
| 4 | 2105010118 | 2019-07-22T20:15:57 | 24.41 | 162 | 10.33 |
| 5 | 2105010120 | 2019-07-24T06:16:41 | 112.83 | 95 | 7.97 |
| 6 | 2105010120 | 2019-07-24T06:16:41 | 155.12 | 162 | 7.97 |
| 7 | 2105010127 | 2019-09-01T10:11:00 | 43.51 | 162 | 9.48 |
| 8 | 2105010144 | 2020-01-12T00:52:20 | 90.77 | 202 | 25.59 |
| 9 | 2105010151 | 2020-01-19T00:11:20 | 89.39 | 158 | 12.45 |
| 10 | 2105010154 | 2020-01-22T01:03:32 | 60.61 | 144 | 9.99 |
| 11 | 2105010158 | 2020-02-14T00:37:00 | 51.91 | 142 | 7.60 |

Table 5.1: Table contains list of observations from 4U 1323-62 where the clear presence of bursts were confirmed and information regarding their respective bursts. There are total 11 bursts (Figure 5.7 to Figure 5.17). Date and time of observation, duration of burst, peak intensity, persistent intensity are mentioned in the table.

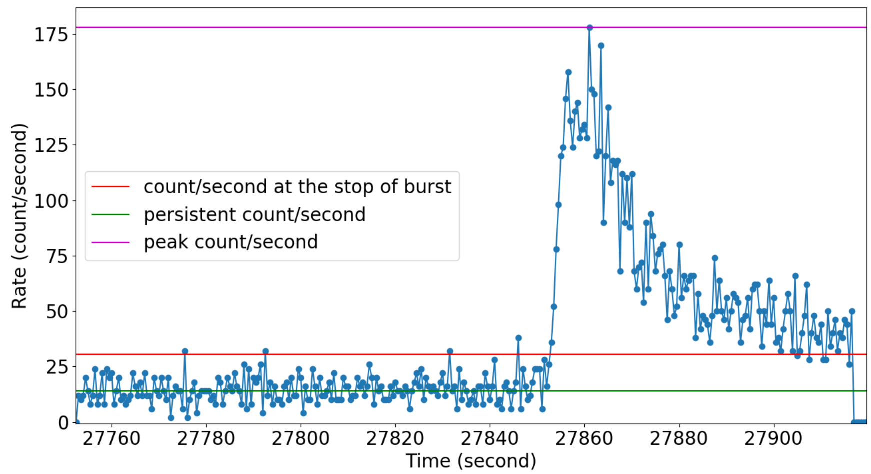


Figure 5.7: The zoomed light curve of thermonuclear burst from source 4U 1323–62 obtained from the observation ID 1105010142. Example of cut burst (Observation date: 2018-01-12, Observation start time: 04:04:57 taking a time bin size of 0.5 s.(Table 5.1)).

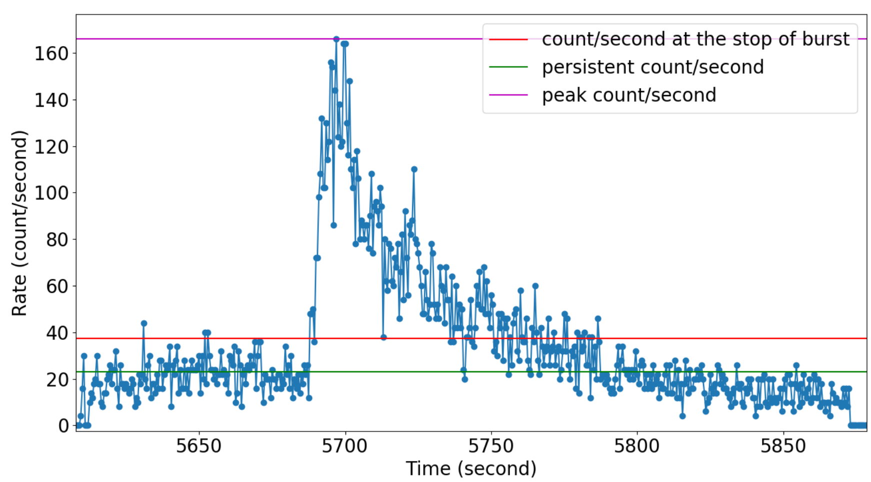


Figure 5.8: The zoomed light curve of thermonuclear burst from source 4U 1323–62 obtained from the observation ID 1105010165 (Observation date: 2019-02-28, Observation start time: 06:55:55 taking a time bin size of 0.5 s. (Table 5.1)).

burst 1105010165 over complete NICER energy range, peaks at ~ 10 s. For 0.2-2 keV (Figure 5.19) energy range, the photon counts does not change

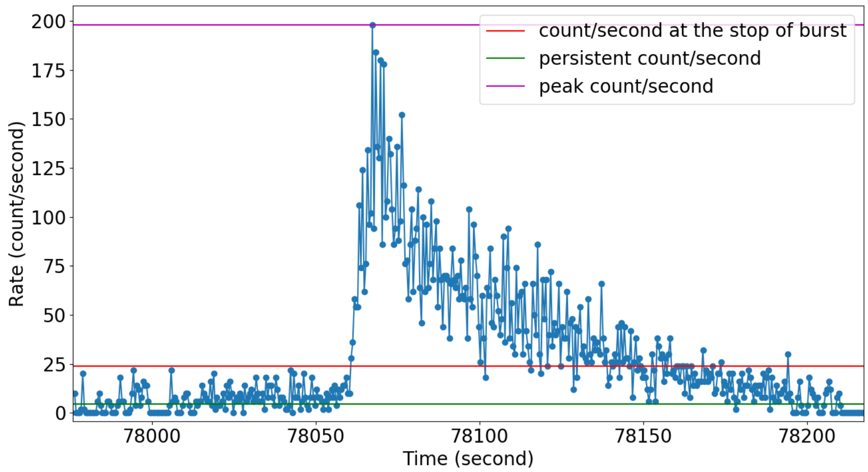


Figure 5.9: The zoomed light curve of thermonuclear burst from source 4U 1323–62 obtained from the observation ID 2105010114 (Observation date: 2019-07-17, Observation start time: 01:20:16 taking a time bin size of 0.5 s. (Table 5.1)).

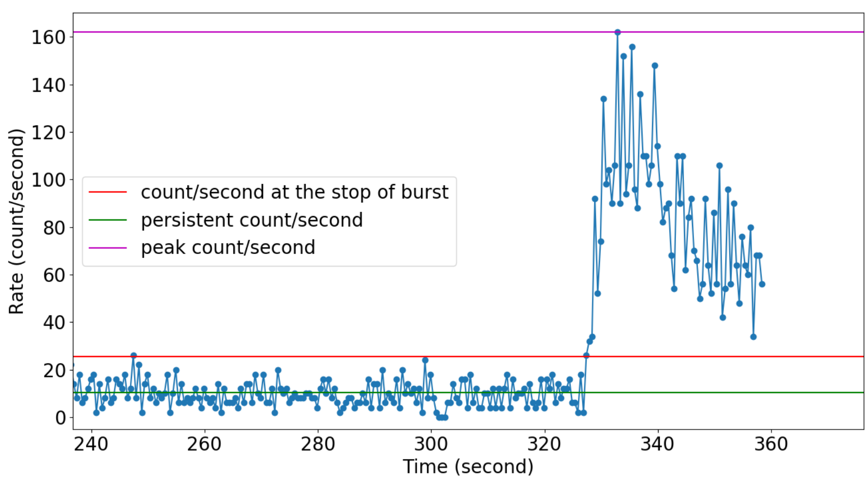


Figure 5.10: The zoomed light curve of thermonuclear burst from source 4U 1323–62 obtained from the observation ID 2105010118. (Observation date: 2019-07-22, Observation start time: 20:15:57 taking a time bin size of 0.5 s.) This is example of the cut burst and the observation is also of very low exposure compared to other observations (Table 5.1).

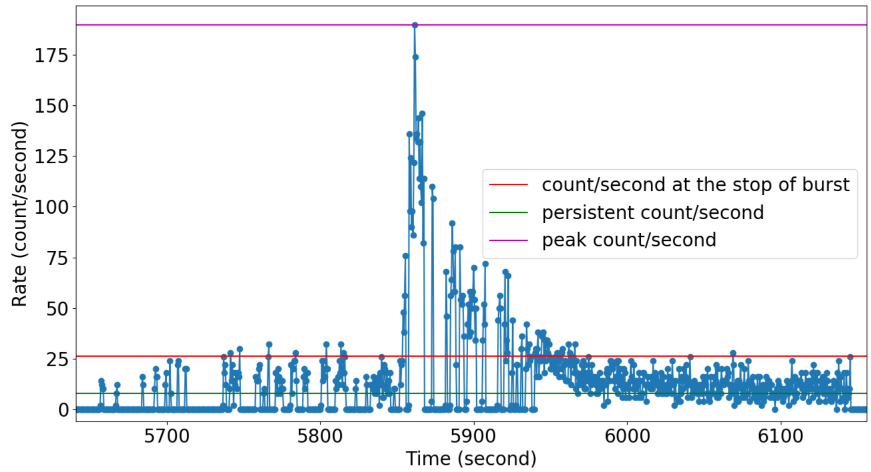


Figure 5.11: The zoomed light curve of thermonuclear burst from source 4U 1323–62 obtained from the observation ID 2105010120, two bursts were detected. This is first burst (Observation date: 2019-07-24, Observation start time: 06:16:41 taking a time bin size of 0.5 s.). This is example of the burst light curve where there are data gaps. (Table 5.1).

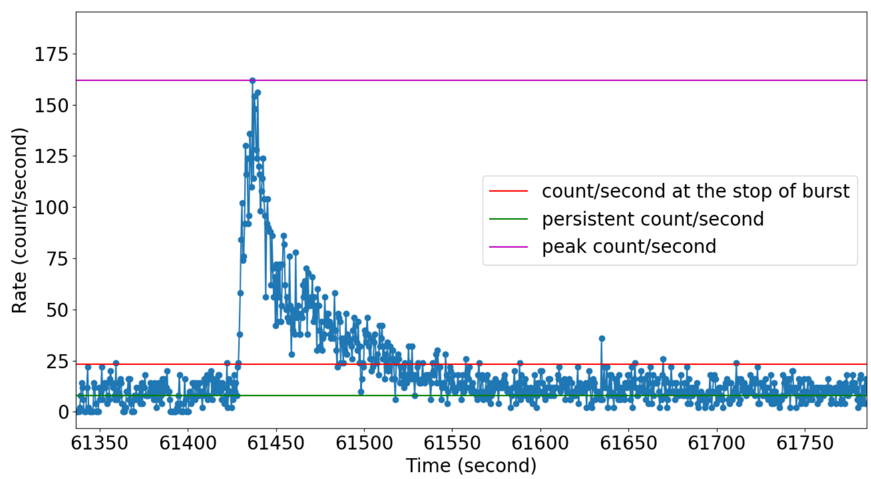


Figure 5.12: The zoomed light curve of thermonuclear burst from source 4U 1323–62 obtained from the observation ID 2105010120, two bursts were detected. This is second burst (Observation date: 2019-07-24, Observation start time: 06:16:41 taking a time bin size of 0.5 s. (Table 5.1)).

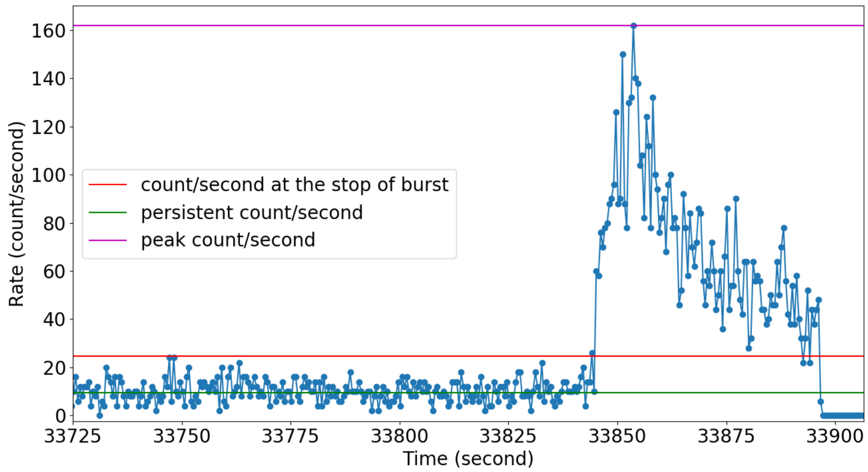


Figure 5.13: The zoomed light curve of thermonuclear burst from source 4U 1323–62 obtained from the observation ID 2105010127. (Observation date: 2019-09-01, Observation start time: 10:11:00 taking a time bin size of 0.5 s.) It is an example of cut burst. (Table 5.1).

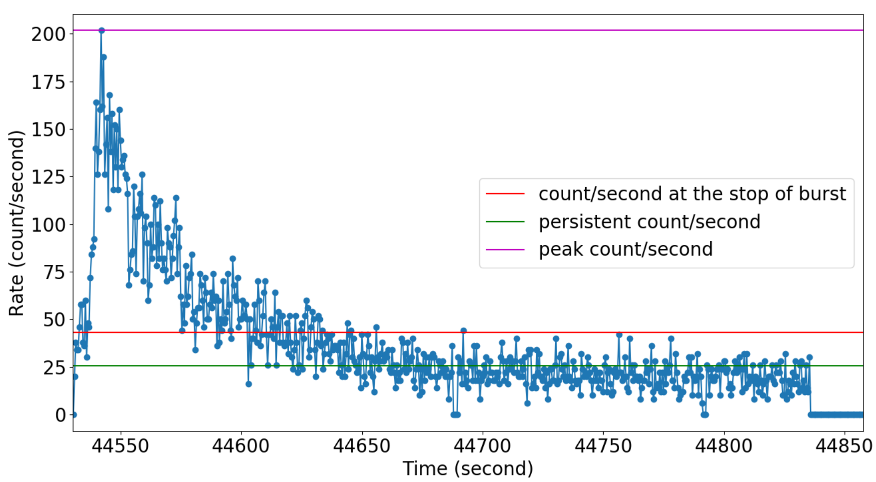


Figure 5.14: The zoomed light curve of thermonuclear burst from source of 4U 1323–62 obtained from the observation ID 2105010144. (Observation date: 2020-01-12, Observation start time: 00:52:20 taking a time bin size of 0.5 s.) It is an example where burst is at the start of orbit. (Table 5.1).

much over the entire burst. As we go to 2-3 keV (Figure 5.20) energy range, we start to observe that the photon count at the peak decay with time. The

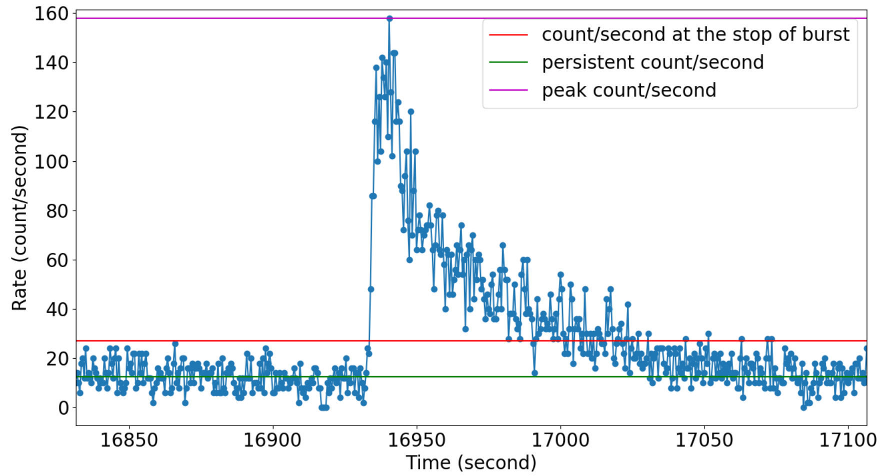


Figure 5.15: The zoomed light curve of thermonuclear burst from source 4U 1323–62 obtained from the observation ID 2105010151. (Observation date: 2020-01-19, Observation start time: 00:11:20 taking a time bin size of 0.5 s. (Table 5.1)).

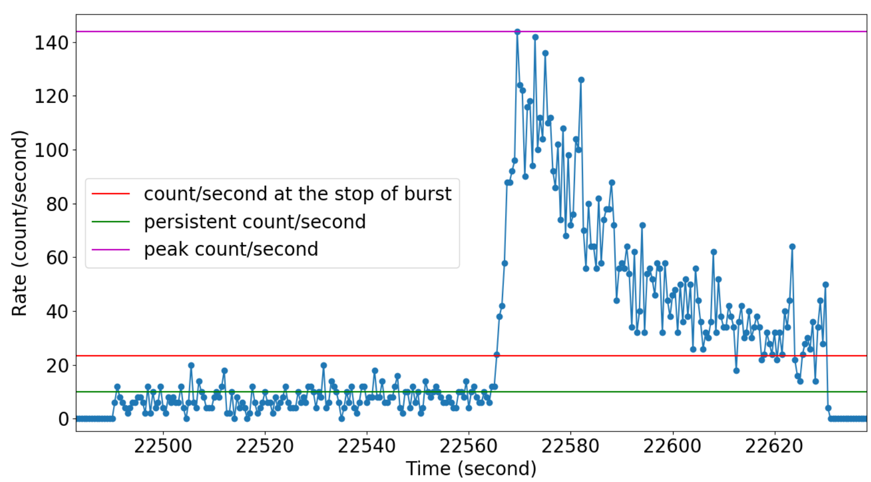


Figure 5.16: The zoomed light curve of thermonuclear burst from source 4U 1323–62 obtained from the observation ID 2105010154 (Observation date: 2020-01-22, Observation start time: 01:03:32 taking a time bin size of 0.5 s.). It is an example of cut burst (Table 5.1)).

sharp decay is observed in photon counts in 3-5 keV range after the peak (Figure 5.21 and Figure 5.22). The photon count is maximum in this energy

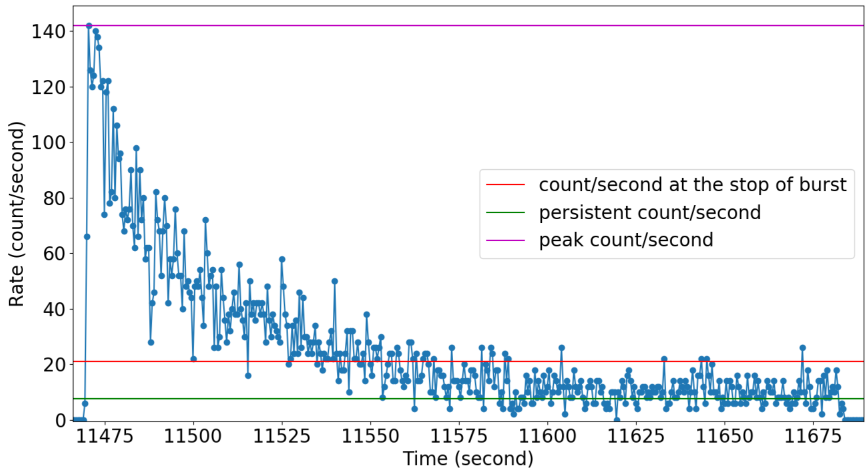


Figure 5.17: The zoomed light curve of thermonuclear burst from source 4U 1323–62 obtained from the observation ID 2105010158. (Observation date: 2020-02-14, Observation start time: 00:37:00 taking a time bin size of 0.5 s.). It is an example of cut burst. (Table 5.1).

range at the peak of the burst. After 5-6 keV (Figure 5.23) we again start to see the decrease in photon count at peak as we move to 6-7 keV (Figure 5.23) energy range.

## 5.2 Time-resolved spectroscopy

We performed the time resolved spectroscopy to study the evolution of burst spectrum with time. For doing time-resolved spectroscopy we generated unequal time bins using python code such that each bin would be having minimum of 300 counts excluding the persistent count contribution. In this way the entire burst was covered. For each such interval we created a spectrum file. We used grppha command to group the burst spectrum, we used grouping criterion of 10 which means that each channel must contain minimum of 10 photons. Also, we added to it background corrections (on actual spectrum) as well as correction related to instrument (on the model we used for fitting) using background file (persistent emission spectrum), and ARF and RMF files (contains detector response files) respectively. The ARF and RMF files are not the correction on the observed spectrum but

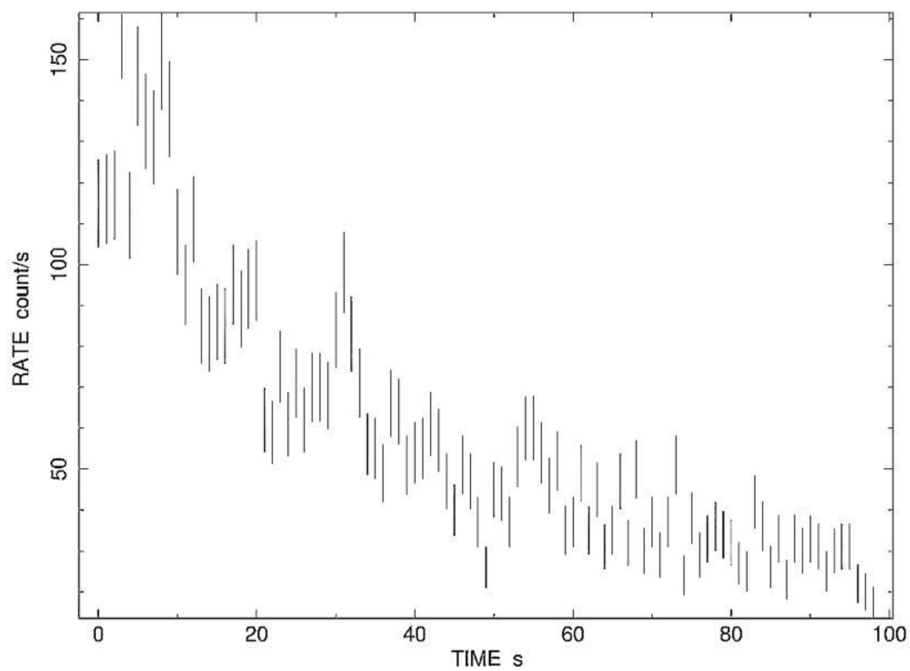


Figure 5.18: The zoomed light curve of thermonuclear burst from source 4U 1323–62 obtained from the observation ID 1105010165 (Observation date: 2019-02-28, Observation start time: 06:55:55 taking a time bin size of 1.0 s). Energy range is 0.2-12 keV.

on the model we are using for fitting. The process of deleting the detector response completely from the observed spectrum is often tricky. So rather than deleting it from the observed spectrum, we prefer to convolve it with the model used for fitting.

The software XSpec was used for the generating the spectrum. We considered that the spectrum can be well described by the blackbody model. So we fitted our spectrum with the blackbody model. We use the abund command in XSpec, to set values for abundances of different elements in interstellar medium from Wilms et al. (2000). We used Tuebingen-Boulder ISM absorption model to take into account absorption due to interstellar medium which is a multiplicative model with the black body model. Our total model is tbabs * bbodyrad. An example of the spectrum fitted with

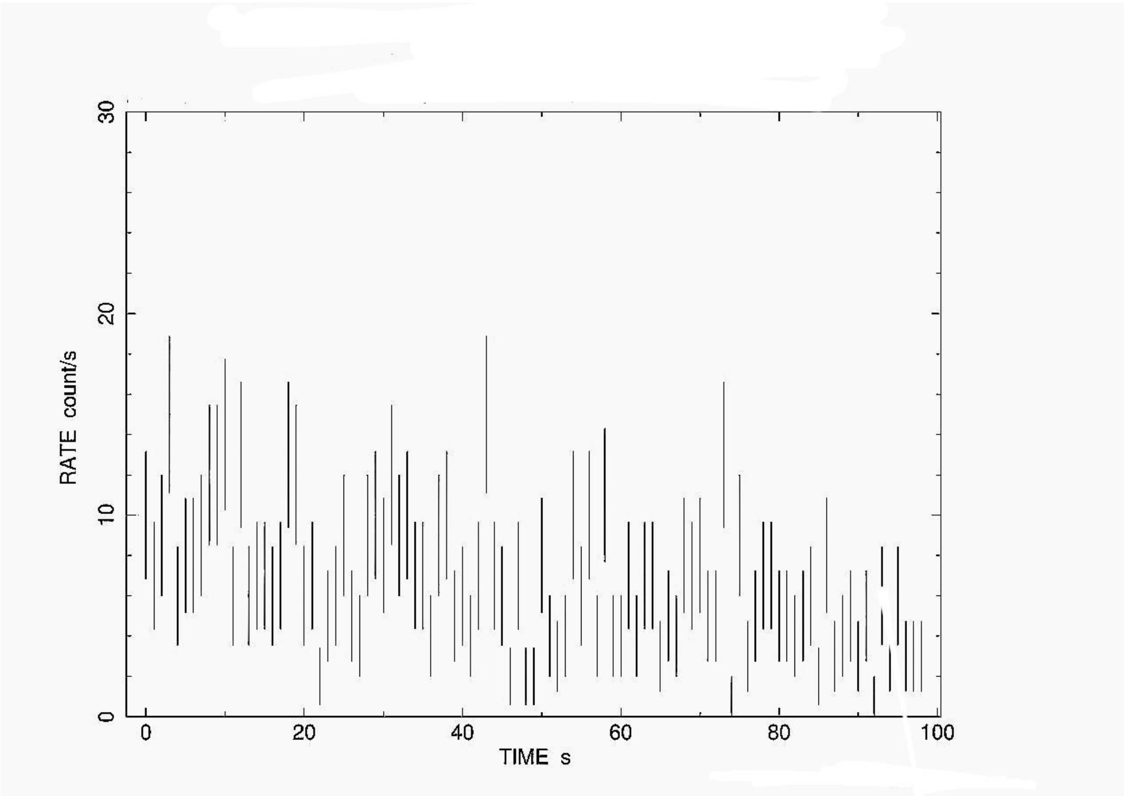


Figure 5.19: The energy resolved zoomed light curve of thermonuclear burst from source 4U 1323–62 obtained from the observation ID 1105010165 (Observation date: 2019-02-28, Observation start time: 06:55:55 taking a time bin size of 1.0 s). Energy range is 0.2-2 keV.

our model is in Figure 5.25. The systematic error was set to 15%. The model fits nicely with our spectrum (reduced chi square in range ~ (0.6-0.7)). The parameter for neutral hydrogen density was kept constant while other parameters were varied. The value for neutral hydrogen density was taken as $4 \times 10^{22}\ cm^{-2}$ (Boirin et al. 2005). We plotted flux, temperature, and blackbody radius with respect to time to see how they change with time (Figure 5.26 to Figure 5.36), the energy ranges were 0.2-7 and 0.5-7 keV. We observe that the flux, temperature, and radius variation with time for our case is the same as that of a typical burst. We see that flux and temperature show similar variations, i.e., near the peak of the burst, temperature becomes maximum and decreases with time. During the peak, the radius of the blackbody is small. When the flame starts to spread over the surface we see an increase in blackbody radius and after some time its radius starts

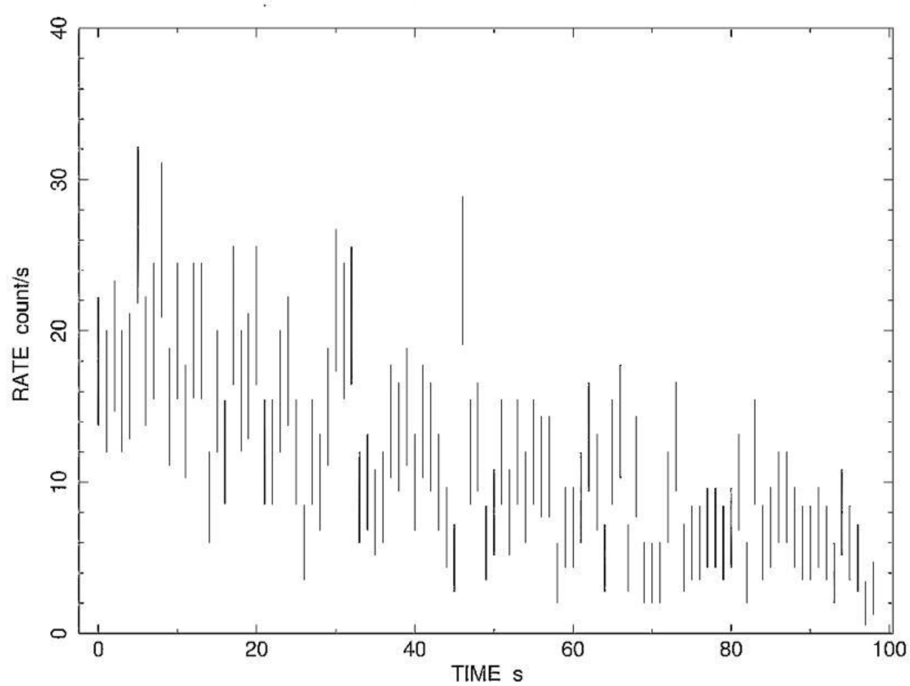


Figure 5.20: The energy resolved zoomed light curve of thermonuclear burst from source 4U 1323–62 obtained from the observation ID 1105010165 (Observation date: 2019-02-28, Observation start time: 06:55:55 taking a time bin size of 1.0 s). Energy range is 2-3 keV.

to decrease due to cooling. This typical behaviour is seen in burst no. 1 (Figure 5.26),3 (Figure 5.28),5 (Figure 5.30),7 (Figure 5.32),9 (Figure 5.34), 10 (Figure 5.35). Burst no 2 (Figure 5.27) and 6 (Figure 5.31) show a rise in flux near the cooling tail. For burst no. 4 (Figure 5.29) we see that third point in panel no. 2 and 3 are not nicely fitted. The same case of poor fit is observed in the second point in the middle panel for burst no. 8 (Figure 5.33).

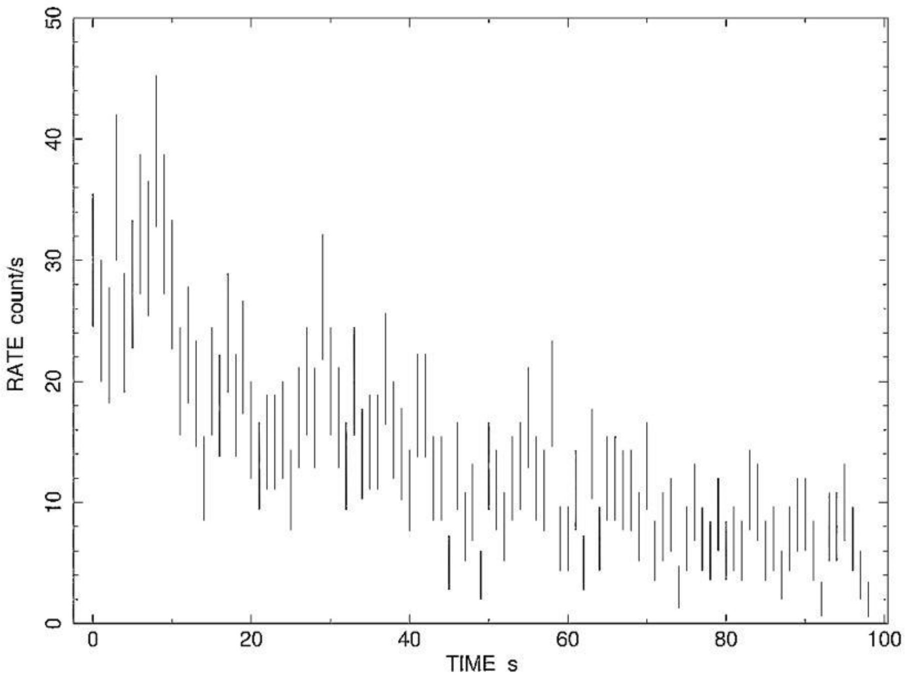


Figure 5.21: The energy resolved zoomed light curve of thermonuclear burst from source 4U 1323–62 obtained from the observation ID 1105010165 (Observation date: 2019-02-28, Observation start time: 06:55:55 taking a time bin size of 1.0 s). Energy range is 3-4 keV.

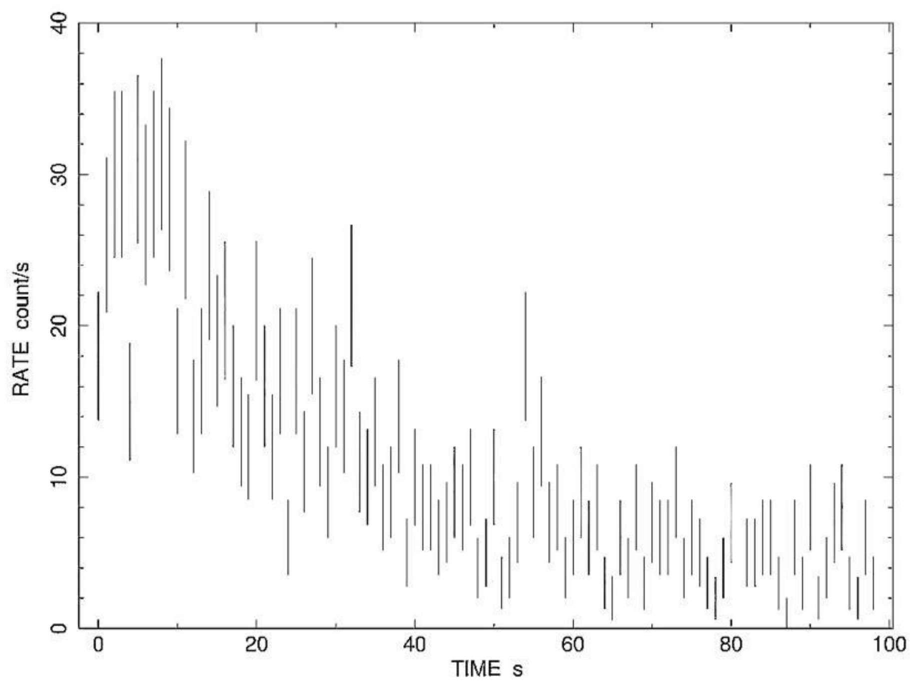


Figure 5.22: The energy resolved zoomed light curve of thermonuclear burst from source 4U 1323–62 obtained from the observation ID 1105010165 (Observation date: 2019-02-28, Observation start time: 06:55:55 taking a time bin size of 1.0 s). Energy range is 4-5 keV.

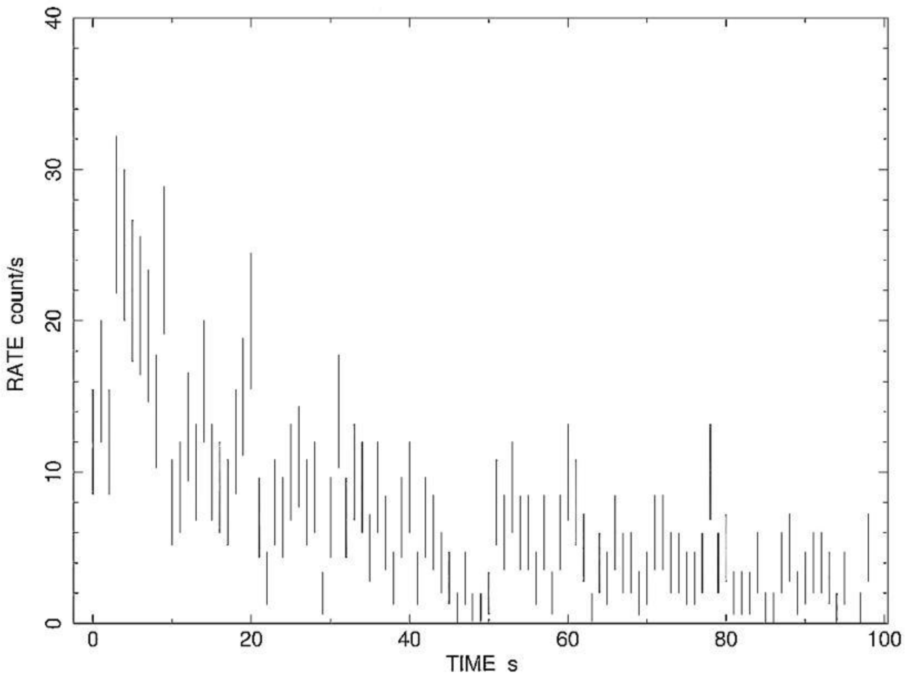


Figure 5.23: The energy resolved zoomed light curve of thermonuclear burst from source 4U 1323–62 obtained from the observation ID 1105010165 (Observation date: 2019-02-28, Observation start time: 06:55:55 taking a time bin size of 1.0 s). Energy range is 5-6 keV.

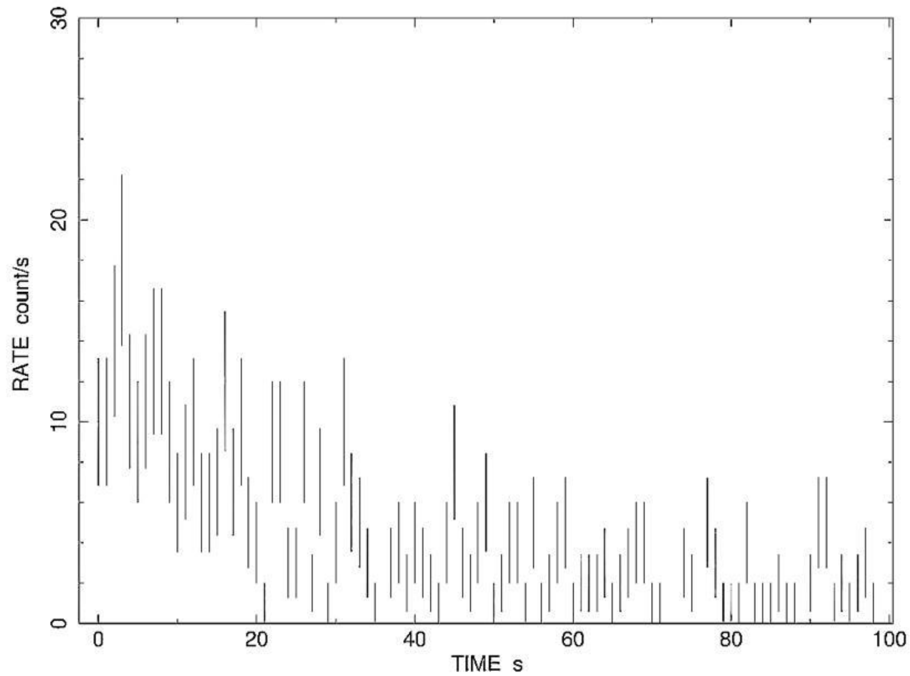


Figure 5.24: The energy resolved zoomed light curve of thermonuclear burst from source 4U 1323–62 obtained from the observation ID 1105010165 (Observation date: 2019-02-28, Observation start time: 06:55:55 taking a time bin size of 1.0 s). Energy range is 6-7 keV.

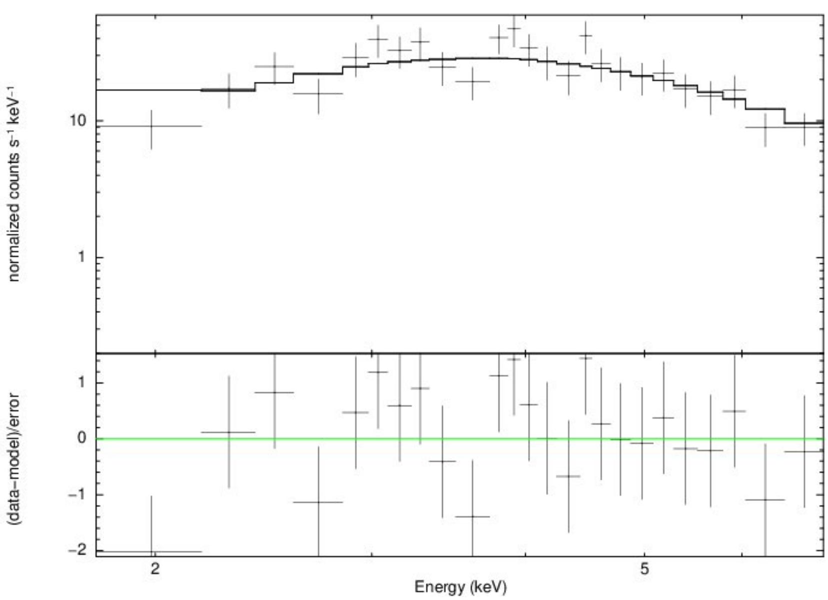


Figure 5.25: The spectrum of first 3.5 s of the burst generated using XSpec in energy range 1-7 keV. The fitting is done using [tbabs*(bbodyrad)] model. Upper panel- cross indicates actual data point. Solid line indicates fitted model. Lower panel- cross indicates residuals.

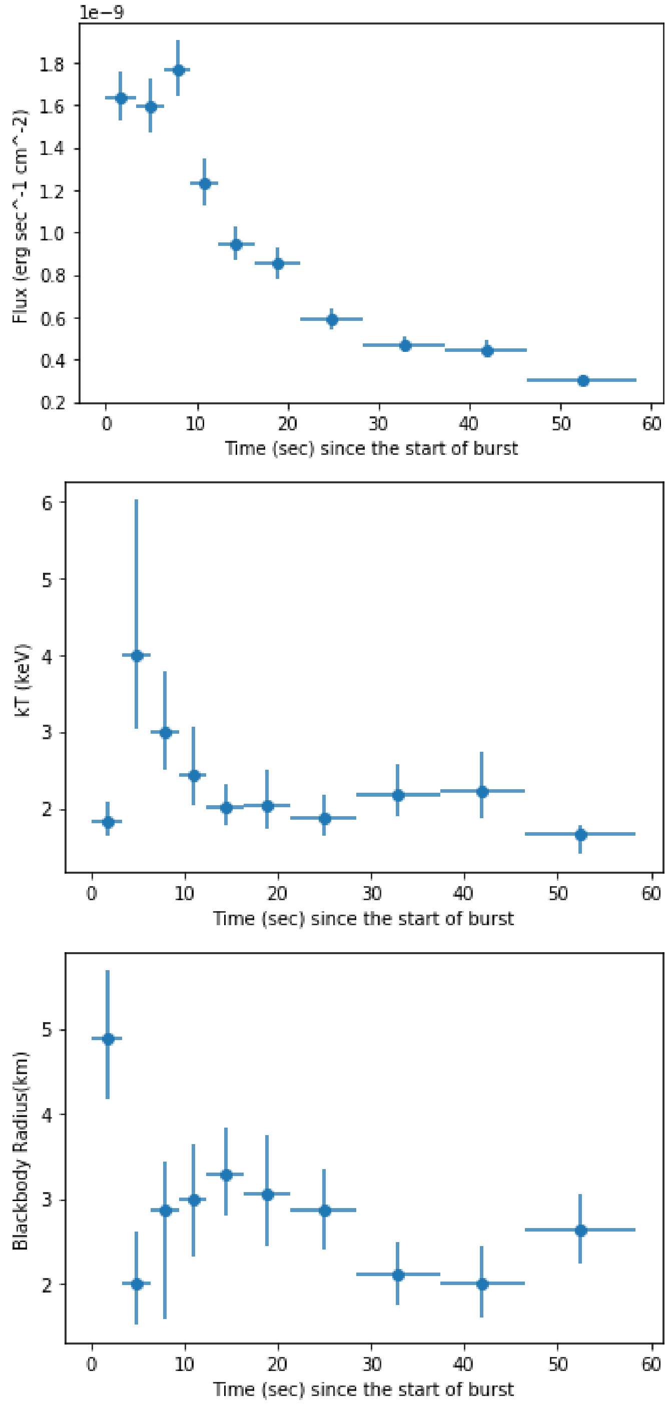


Figure 5.26: The plots indicate how the parameters of the blackbody model fitted to the burst spectrum changes with time for burst no. 1 (Table 5.1). Upper panel- Flux vs. Time. Flux ranges from 0.2-7.0 keV and flux scale is in unit of $10^{-9}$ erg $s^{-1}$ $cm^{-2}$. Middle panel- Blackbody temperature vs. Time. Third panel- Blackbody radius vs. Time.

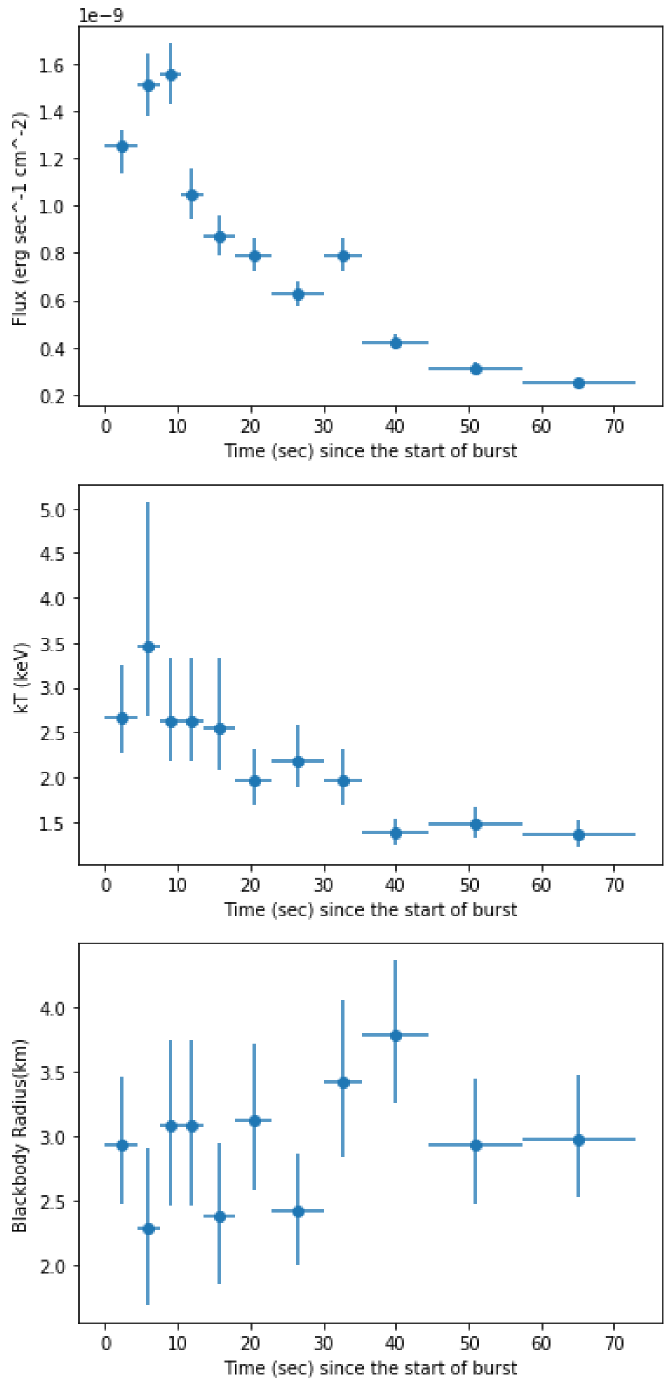


Figure 5.27: The plots indicate how the parameters of the blackbody model fitted to our burst spectrum changes with time for burst no. 2 (Table 5.1). Upper panel- Flux vs. Time. Flux ranges from 0.2-7.0 keV and flux scale is in unit of $10^{-9}$ erg $s^{-1}$ $cm^{-2}$. Middle panel- Blackbody temperature vs. Time. Third panel- Blackbody radius vs. Time.

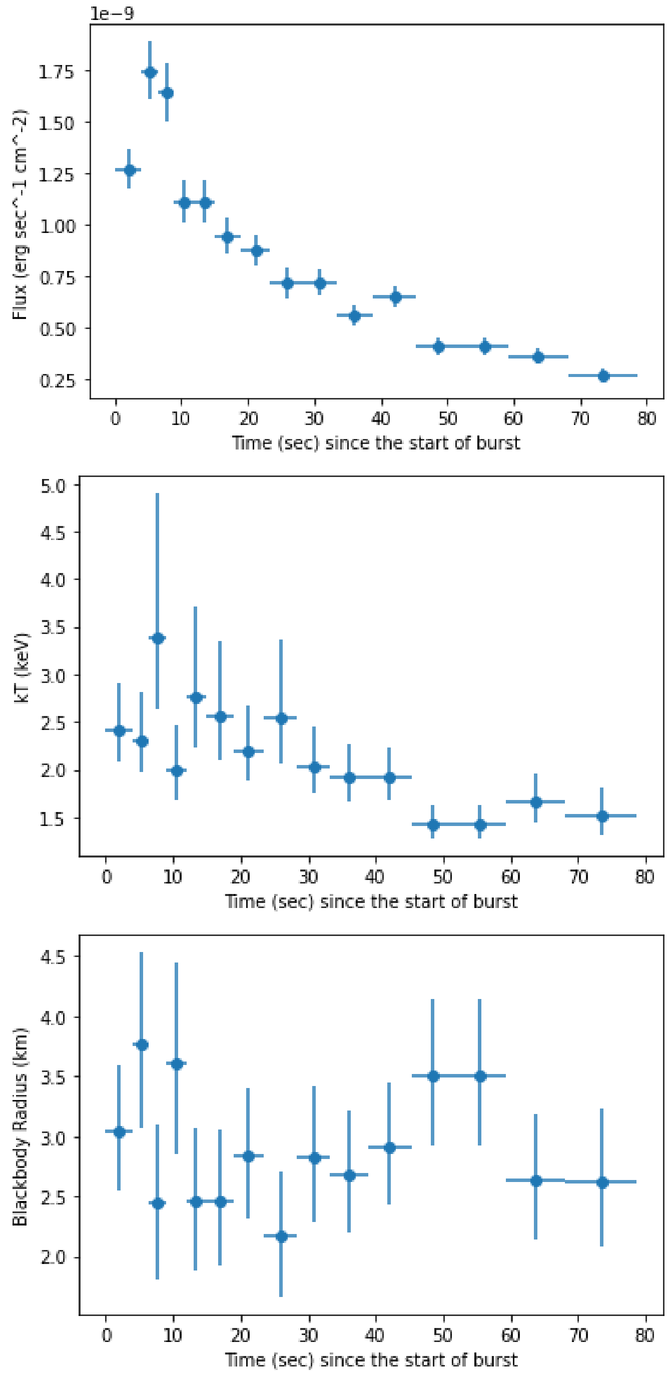


Figure 5.28: The plots indicate how the parameters of the blackbody model fitted to our burst spectrum changes with time for burst no. 3 (Table 5.1). Upper panel- Flux vs. Time. Flux ranges from 0.2-7.0 keV and flux scale is in unit of $10^{-9}$ erg $s^{-1}$ $cm^{-2}$. Middle panel- Blackbody Temperature vs. Time. Third panel- Blackbody radius vs. Time.

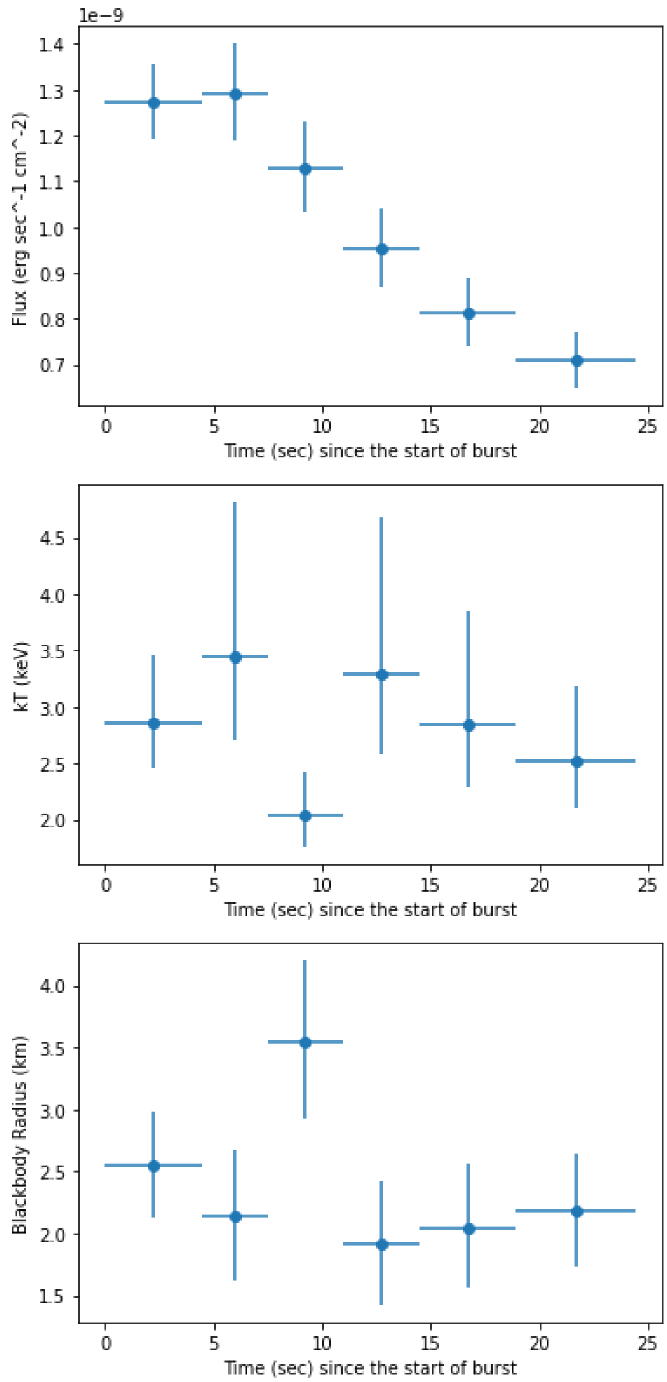


Figure 5.29: The plots indicate how the parameters of the blackbody model fitted to our burst spectrum changes with time for burst no. 4 (Table 5.1). Upper panel- Flux vs. Time. Flux ranges from 0.2-7.0 keV and flux scale is in unit of $10^{-9}$ erg $s^{-1}$ $cm^{-2}$. Middle panel- Temperature vs. Time. Third panel- Blackbody radius vs. Time.

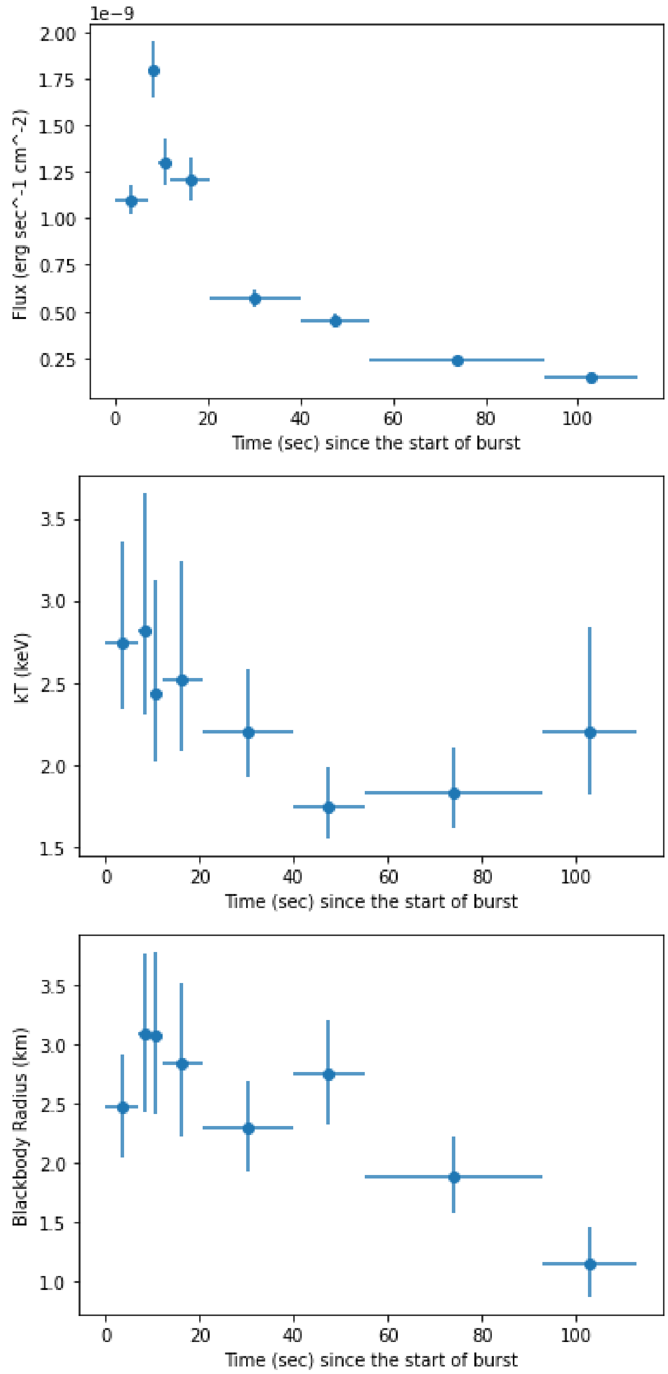


Figure 5.30: The plots indicate how the parameters of the blackbody model fitted to our burst spectrum changes with time for burst no. 5 (Table 5.1). Upper panel- Flux vs. Time. Flux ranges from 0.5-7.0 keV and flux scale is in unit of $10^{-9}$ erg $s^{-1}$ $cm^{-2}$. Middle panel- Blackbody Temperature vs. Time. Third panel- Blackbody radius vs. Time.

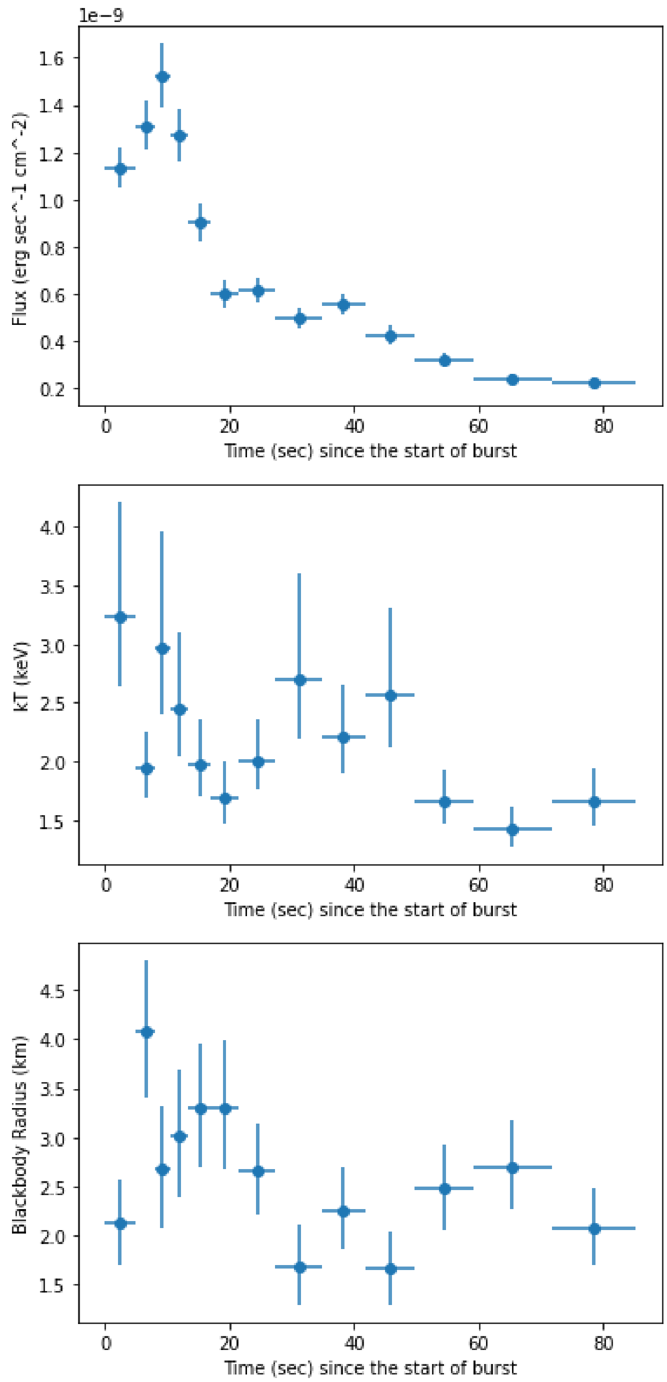


Figure 5.31: The plots indicate how the parameters of the blackbody model fitted to our burst spectrum changes with time for burst no. 6 (Table 5.1). Upper panel- Flux vs. Time. Flux ranges from 0.5-7.0 keV and flux scale is in unit of $10^{-9}$ erg $s^{-1}$ $cm^{-2}$. Middle panel- Blackbody Temperature vs. Time. Third panel- Blackbody radius vs. Time.

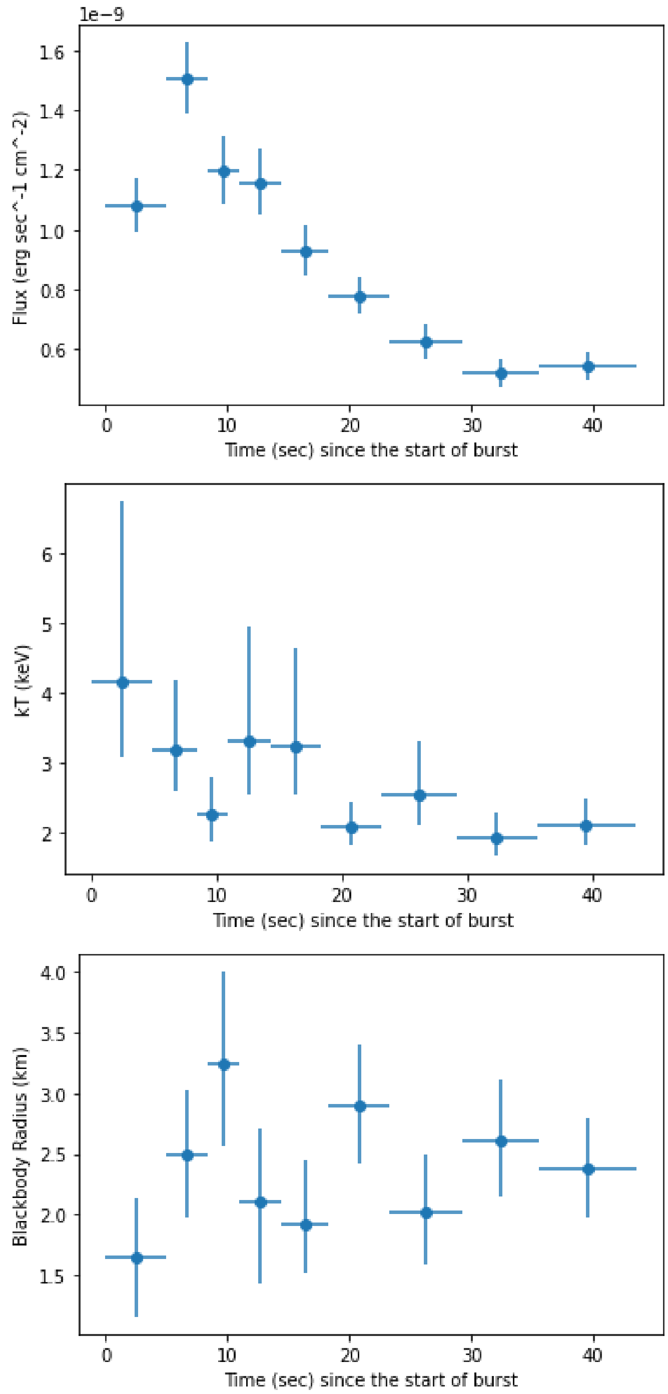


Figure 5.32: The plots indicate how the parameters of the blackbody model fitted to our burst spectrum changes with time for burst no. 7 (Table 5.1). Upper panel- Flux vs. Time. Flux ranges from 0.2-7.0 keV and flux scale is in unit of $10^{-9}$ erg $s^{-1}$ $cm^{-2}$. Middle panel- Blackbody Temperature vs. Time. Third panel- Blackbody radius vs. Time.

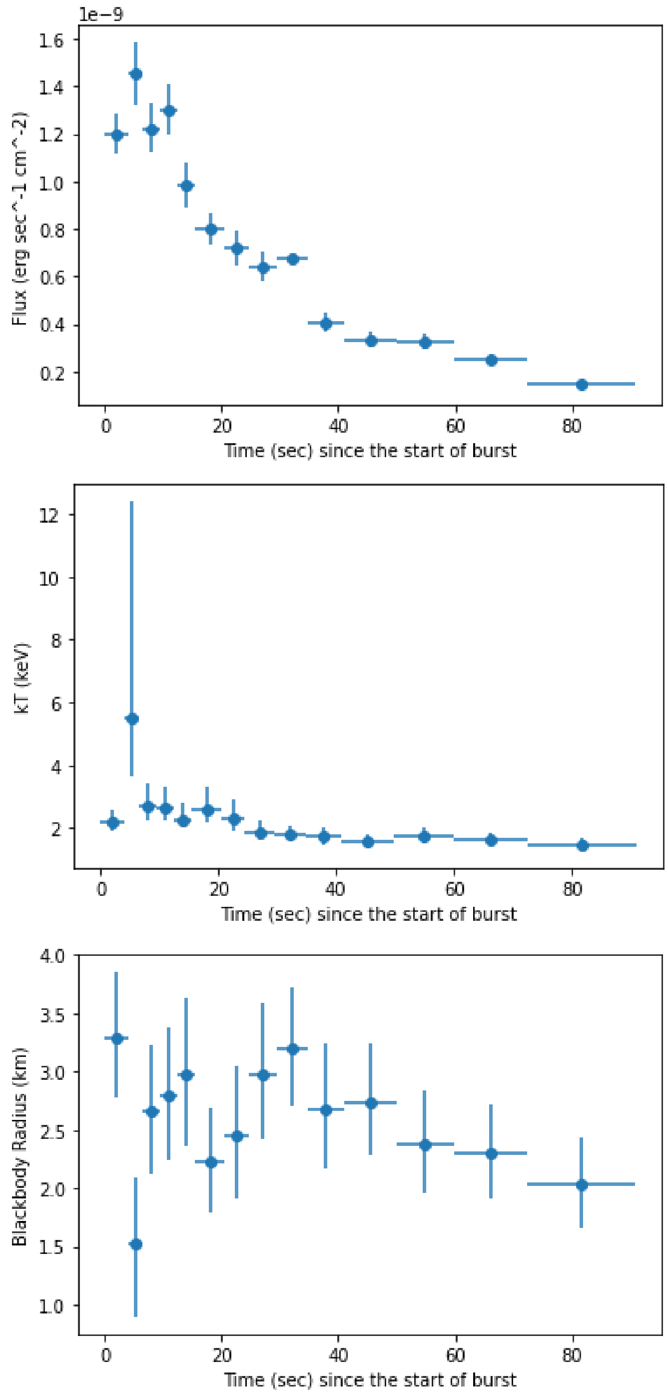


Figure 5.33: The plots indicate how the parameters of the blackbody model fitted to our burst spectrum changes with time for burst no. 8 (Table 5.1). Upper panel- Flux vs. Time. Flux ranges from 0.5-7.0 keV and flux scale is in unit of $10^{-9}$ erg $s^{-1}$ $cm^{-2}$. Middle panel- Blackbody Temperature vs. Time. Third panel- Blackbody radius vs. Time.

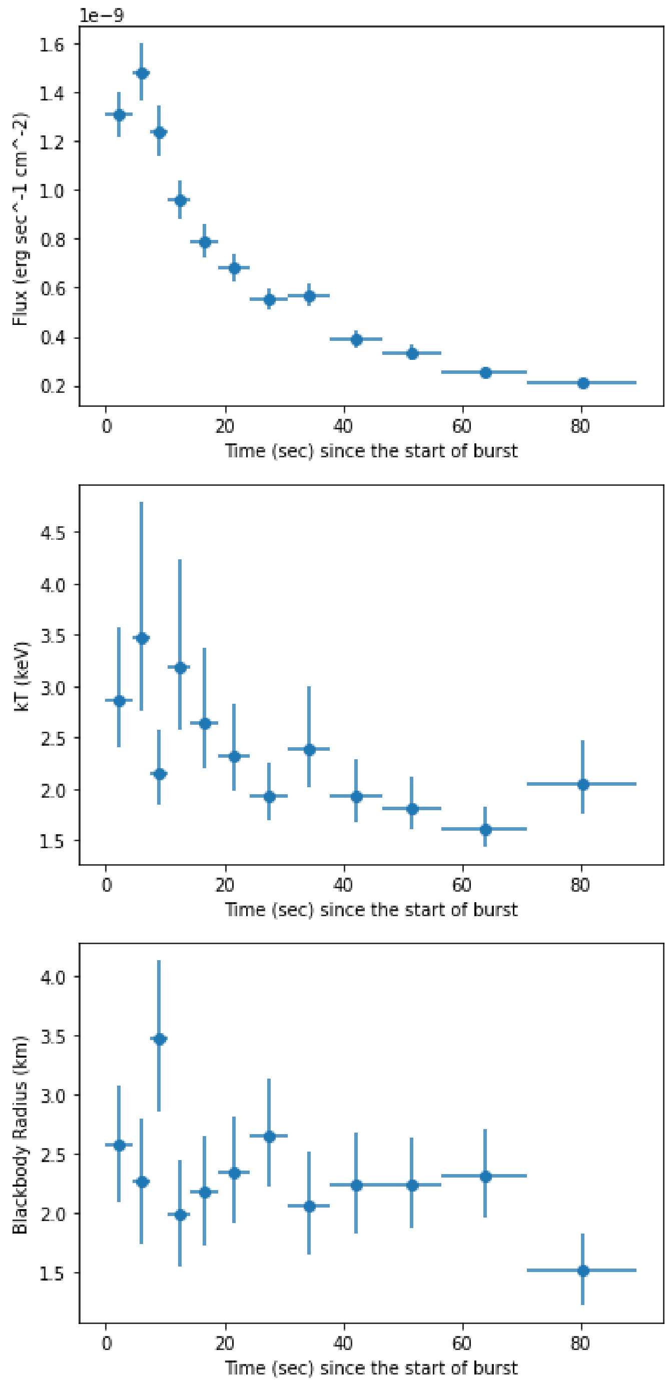


Figure 5.34: The plots indicate how the parameters of the blackbody model fitted to our burst spectrum changes with time for burst no. 9 (Table 5.1). Upper panel- Flux vs. Time. Flux ranges from 0.5-7.0 keV and flux scale is in unit of $10^{-9}$ erg $s^{-1}$ $cm^{-2}$. Middle panel- Blackbody temperature vs. Time. Third panel- Blackbody radius vs. Time.

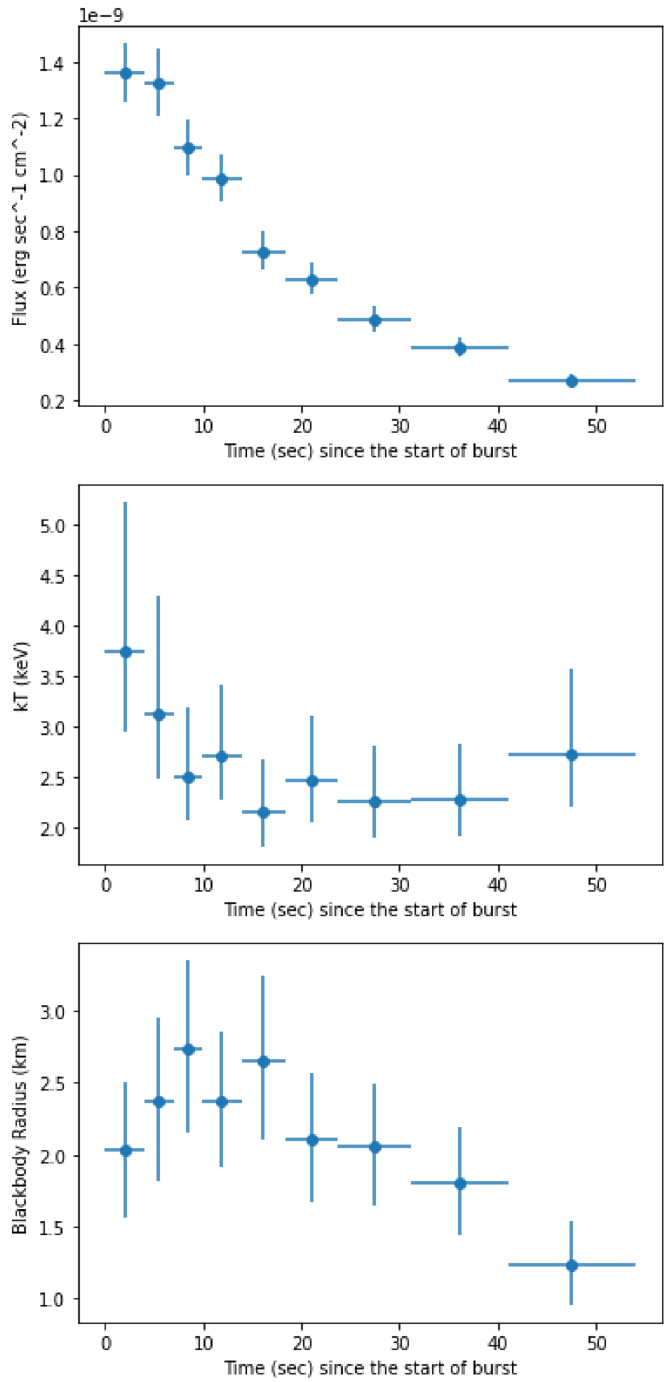


Figure 5.35: The plots indicate how the parameters of the blackbody model fitted to our burst spectrum changes with time for burst no. 10 (Table 5.1). Upper panel- Flux vs. Time. Flux ranges from 0.5-7.0 keV and flux scale is in unit of $10^{-9}$ erg $s^{-1}$ $cm^{-2}$. Middle panel- Blackbody temperature vs. Time. Third panel- Blackbody radius vs. Time.

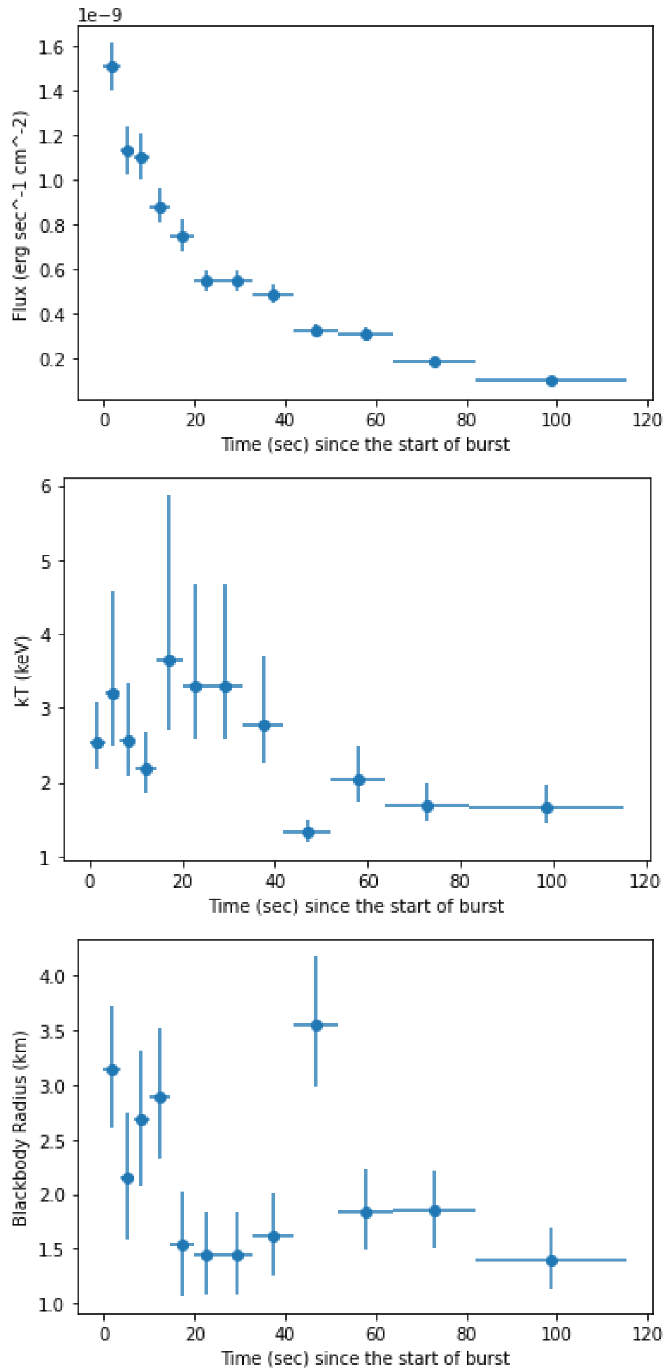


Figure 5.36: The plots indicate how the parameters of the blackbody model fitted to our burst spectrum changes with time for burst no. 11 (Table 5.1). Upper panel- Flux vs. Time. Flux ranges from 0.2-7.0 keV and flux scale is in unit of $10^{-9}$ erg $s^{-1}$ $cm^{-2}$. Middle panel- Blackbody temperature vs. Time. Third panel- Blackbody radius vs. Time.

# Chapter 6

# Discussion and conclusion

In this work we studied the source 4U 1323-62, the observations were taken using XTE (X-ray Timing Instrument) mounted on NICER telescope. We were able to obtain a light curve for 92 bursts out of 120 observations. Out of them we found 11 burst candidates. We performed Time resolved spectroscopy on the burst to see how the spectrum changes with time. Black body model was used for spectral fitting. We found that flux during the burst is in the range $\sim 0.2 - 1.8\times\ 10^{-9}$ erg $s^{-1}\ \ cm^{-2}$, the blackbody temperature ranges as $\sim$ 1.3 – 4 keV, and blackbody radius is in range $\sim$ 1-5 km. The blackbody temperature and blackbody radius of the bursts listed in Galloway et al. 2008 is $\sim$ 1.5 – 2.5 keV and $\sim$ 1 – 6.5 km respectively. The range of blackbody temperature and blackbody radius in the work Bhulla et al. 2020 is $\sim$ 0.7 – 3.05 keV and $\sim$ 55 – 80 km respectively. We can conclude that the bursts covered in this work is having higher blackbody temperature compared to previous work and the radius of blackbody is in range somewhat similar to Galloway et al. 2008.

The energy resolved light curves were generated for the burst observed in observation 1105010165 (Figure 5.19 to Figure 5.24). We can observe that the most of the photon counts during the peak of the burst are contributed by the photons at higher energies, i.e., 3-7 keV. We conclude that it is due to higher temperature during the peak of the burst which causes the energy of the photon to go towards the higher end.

The source 4U 1323-62 has been previously studied by different telescopes. The dip in flux was detected during the burst for this source (van der Klis et al. 1985). The presence of dip was suggested to be due to high inclination angle ~ 60-80 degrees (angle between rotation axis and line of sight) (Frank 1987, Bhulla et al. 2020). The photospheric radius expansion was detected for this source in previous work (Bhulla et al. 2020). The presence of double burst and faint secondary burst were also observed for this source (Galloway et al. 2008).

For observation 1105010165, (Figure 5.18) at ~ 30 seconds we can see a rise in photon count. The possibility to consider here is flame stalling due to Coriolis force. We can consider that fuel is covering most of the surface of the burst. Now as the burning front is moving towards the equator, it is stalled due to Coriolis force. The stalling of the burning front causes cooling of the hot regions which causes less flux. As it approaches very near the equator, the burning front again speeds up, and we notice a rise in flux (Bhattacharyya & Strohmayer 2006). This behaviour is seen from the parameter vs. time plots (Figure 5.27). The work, Guver et al. (2021), discovered late secondary burst near the tail during cooling phase of primary burst from the source 4U 1608-52. We can say that the rise in photon count we observed is similar to secondary burst discussed in Guver et al. (2021). Another reason to take into account would be that if the accretion rate is high enough, then we can say that after the burst peak, the residual heating conditions set by the burst can ignite a newly formed column of accreted fuel (Guver et al. 2021). The magnetic field also can cause the flame stalling (Guver et al. 2021). For observation 1105010120, second burst, we can see a plateau in the flux plot (upper panel, Figure 5.31). This may be due to the change in thermodynamic conditions, radiative efficiency may get affected due to which we are able to see the plateau like structure in the flux. The bursts detected in this work does not show dips and PRE features as reported in (Bhulla et al. 2020).

To summarize, we studied thermonuclear bursts from the source 4U 1323-62. The time resolved spectroscopy was performed. The blackbody model was used for spectral fitting. When we compared parameter values of blackbody model with the previous work, we observed that upper temperature range in this work is not detected previously for this source. The energy resolved light curves from source 1105010165 showed that energy of photon is dependent on the temperature. For the same observation, we observed the rise in photon counts during the $\sim 30$ s. We said that this behaviour is similar to the secondary peak. We discussed different phenomena which may give rise to this behaviour i.e., Coriolis force, modified ignition conditions and magnetic field. However, to predict exactly the reason behind the secondary peak like behaviour, more complex analysis is needed.

# References


1. Reisenegger, A., 2001, Magnetic Fields Across the Hertzsprung-Russell Diagram, ASP Conference Proceedings, 248, 1

2. Ronald A. Remillard, & Jeffrey. E. McClintock, 2006, ARAA, 44, 8, 9, 10

3. Galloway, D. K., Muno, M. P., Hartman, J. M., Psaltis, D., & Chakrabarty, D. 2008, ApJS, 179, 360

4. C. Sánchez-Fernández, J. J. E. Kajava, J. Poutanen,E. Kuulkers, and V. F. Suleimanov, 2020, A&A, 634, A58, 5

5. Jari J. E. Kajava, Joonas Nattila, Outi-Marja Latvala, Miika Pursiainen, Juri Poutanen, Valery F. Suleimanov, Mikhail G. Revnivtsev, Erik Kuulkers, Duncan K. Galloway, 2014, MNRAS, 6

6. https://heasarc.gsfc.nasa.gov/docs/nicer/mission_guide/

7. Carroll and Ostlie : An introduction to Modern Astrophysics

8. NICER ARCHIVE GUIDE

9. NICER USER GUIDE

10. XSpec user guide

11. Tod Strohmayer and Lars Bildsten, 2003, Compact stellar X-ray sources, ed. W. H. G. Lewin & M. van der Klis, 113, 1, 3, 4, 5, 6, 9

12. Parmar, A. N., Gottwald, M., van der Klis, M., & van Paradijs, J., 1989, ApJ, 338, 1024

13. M. van der Klis, 2004, Compact stellar X-ray sources, Lewin & van der Klis (eds), 1, 6

14. Bhattacharyya, S., & Strohmayer, T. E. 2006, ApJL, 636, L121

15. Tolga Guver, Tugba Boztepe, Ersin Gogus, Manoneeta Chakraborty, Tod E. Strohmayer, Peter Bult, Diego Altamirano, Gaurava K. Jaisawal, Tugce Kocabiyik, C. Malacaria, Unnati Kashyap, Keith C. Gendreau, Zaven Arzoumanian, and Deepto Chakrabarty, 2021, ApJ, 910, 37

16. Boirin, L., Mendez, M., Diaz Trigo, M., Parmar, A., & Kaastra, J. 2005, in SF2A-2005: Semaine de l'Astrophysique Francaise, ed. F. Casoli, T. Contini, J. M. Hameury, & L. Pagani, 443

17. Yashpal Bhulla, Jayashree Roy, S.N.A Jaaffrey, 2020, RAA, 20, 98

18. Frank, J. 1987, Science, 236, 1007

19. Wilms, Allen & McCray, 2000, ApJ, 542, 914

20. van der Klis, M., Jansen, F., van Paradijs, J., & Stollmann, G. 1985, Space Science Reviews, 40, 287